INFORMATION TO USERS

This reproduction was made from a copy of a manuscript sent to us for publication and microfilming. While the most advanced technology has been used to photograph and reproduce this manuscript, the quality of the reproduction is heavily dependent upon the quality of the material submitted. Pages in any manuscript may have indistinct print. In all cases the best available copy has been filmed.

The following explanation of techniques is provided to help clarify notations which may appear on this reproduction.

1. Manuscripts may not always be complete. When it is not possible to obtain missing pages, a note appears to indicate this.

2. When copyrighted materials are removed from the manuscript, a note appears to indicate this.

3. Oversize materials (maps, drawings, and charts) are photographed by sectioning the original, beginning at the upper left hand corner and continuing from left to right in equal sections with small overlaps. Each oversize page is also filmed as one exposure and is available, for an additional charge, as a standard 35mm slide or in black and white paper format.*

4. Most photographs reproduce acceptably on positive microfilm or microfiche but lack clarity on xerographic copies made from the microfilm. For an additional charge, all photographs are available in black and white standard 35mm slide format.*

*For more information about black and white slides or enlarged paper reproductions, please contact the Dissertations Customer Services Department.

UMI University Microfilms International

8613441

Mooney, Jonathan Martin

INVESTIGATION OF THE PROCESS OF INTERNAL PHOTOEMISSION IN PLATINUM SILICIDE SCHOTTKY BARRIER DIODES

The University of Arizona PH.D. 1986

University Microfilms International 300 N. Zeeb Road, Ann Arbor, MI 48106

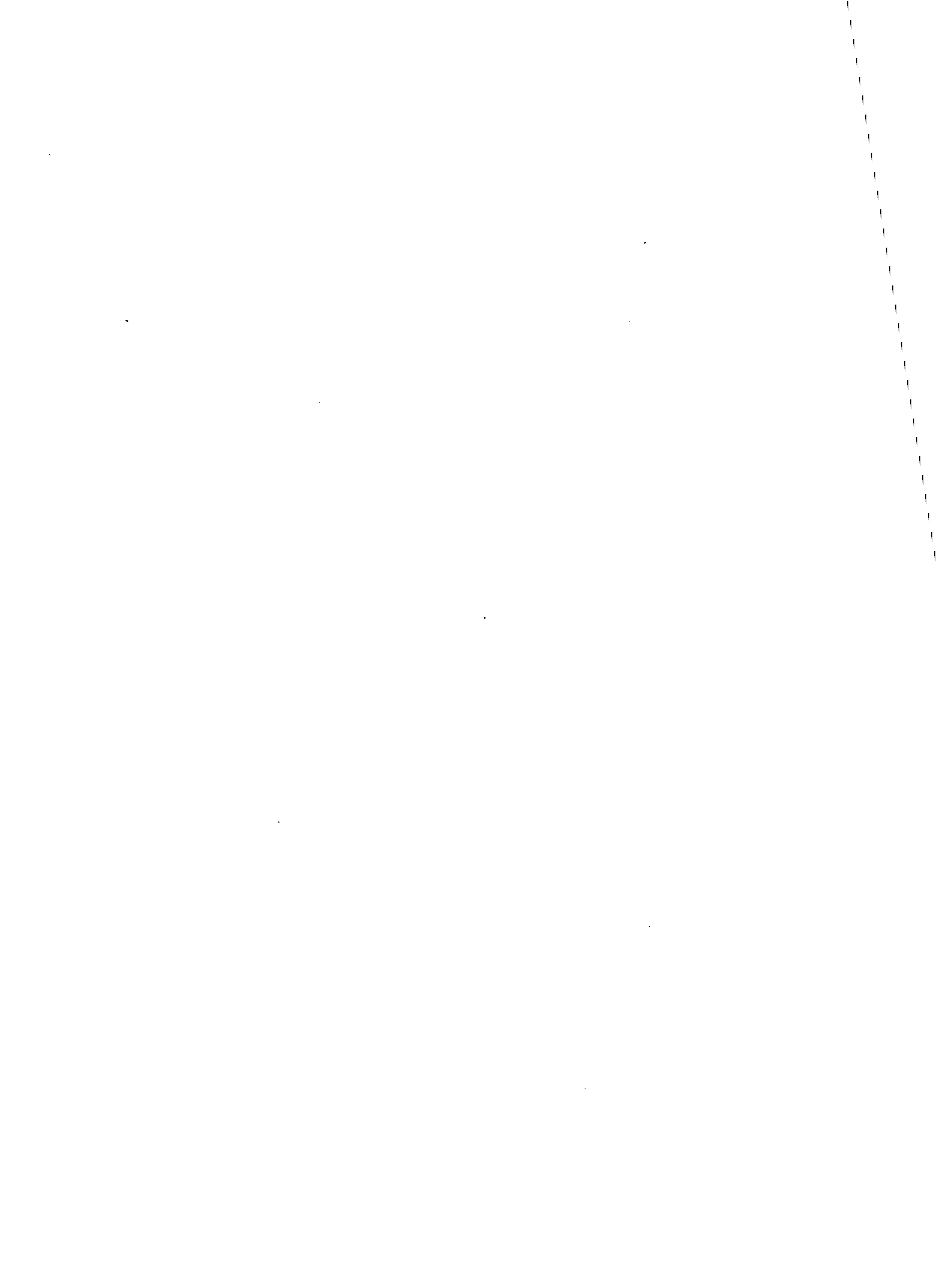

PLEASE NOTE:

In all cases this material has been filmed in the best possible way from the available copy. Problems encountered with this document have been identified here with a check mark ___√___.

1. Glossy photographs or pages ___√___
2. Colored illustrations, paper or print ______
3. Photographs with dark background ___√___
4. Illustrations are poor copy ______
5. Pages with black marks, not original copy ______
6. Print shows through as there is text on both sides of page ______
7. Indistinct, broken or small print on several pages ___√___
8. Print exceeds margin requirements ______
9. Tightly bound copy with print lost in spine ______
10. Computer printout pages with indistinct print ______
11. Page(s) __________ lacking when material received, and not available from school or author.
12. Page(s) __________ seem to be missing in numbering only as text follows.
13. Two pages numbered ______. Text follows.
14. Curling and wrinkled pages ______
15. Dissertation contains pages with print at a slant, filmed as received ________
16. Other ____

University
Microfilms
International

INVESTIGATION OF THE PROCESS OF INTERNAL PHOTOEMISSION IN PLATINUM SILICIDE SCHOTTKY BARRIER DIODES

by

Jonathan Martin Mooney

A Dissertation Submitted to the Faculty of the

COMMITTEE on OPTICAL SCIENCES (GRADUATE)

In Partial Fulfillment of the Requirements
For the Degree of

DOCTOR OF PHILOSOPHY

In the Graduate College

THE UNIVERSITY OF ARIZONA

1 9 8 6

THE UNIVERSITY OF ARIZONA
GRADUATE COLLEGE

As members of the Final Examination Committee, we certify that we have read the dissertation prepared by Jonathan Martin Mooney

entitled Investigation of the process of Internal Photoemission in Platinum Silicide Schottky Barrier Diodes

and recommend that it be accepted as fulfilling the dissertation requirement for the Degree of Doctor of Philosophy.

E. L. Dereniak — Date: Feb 19, 1986

H. H. Barrett — Date: Feb 19, 1986

Ursula Gibson — Date: 2/19/86

F. D. Shepherd — Date: 19 February 1986

Date

Final approval and acceptance of this dissertation is contingent upon the candidate's submission of the final copy of the dissertation to the Graduate College.

I hereby certify that I have read this dissertation prepared under my direction and recommend that it be accepted as fulfilling the dissertation requirement.

Eustace L Dereniak — Feb 19, 1986
Dissertation Director — Date

STATEMENT BY AUTHOR

This dissertation has been submitted in partial fulfillment of requirements for an advanced degree at The University of Arizona and is deposited in the University Library to be made available to borrowers under rules of the Library.

Brief quotations from this dissertation are allowable without special permission, provided that accurate acknowledgment of source is made. Requests for permission for extended quotation from or reproduction of this manuscript in whole or in part may be granted by the head of the major department or the Dean of the Graduate College when in his or her judgment the proposed use of the material is in the interests of scholarship. In all other instances, however, permission must be obtained from the author.

SIGNED: 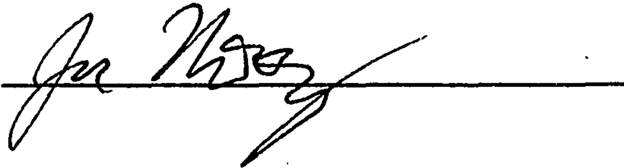

ACKNOWLEDGMENTS

The author would like to express his thanks to Paul W. Pellegrini, Aleksander Golubovic, Davis A. Lange, Charlotte E. Ludington and James J. Murrin of the Rome Air Development Center's Electronic Device Technology Branch for their efforts in the fabrication and measurement of the devices used in this work. He would like to thank Melanie M. Weeks for performing the measurements of the quantum efficiency and dark current, and Linda M. Bouthillette for graphing assistance. The author is grateful to Joseph J. Comer for his Transmission electron microscopy work and for valuable discussions concerning that work.

The author gratefully acknowledges the financial support of the Air Force Office of Scientific Research, Air Force System Command, U. S. Air Force, and the Electron Device Division of Litton Industries.

The author feels indebted to Doctors Eustace L. Dereniak, Freeman D. Shepherd, and Jerry Silverman for their guidance as Research Supervisors, and for their enthusiastic support as friends.

Finally, the author would like to express his gratitude to his parents and grandparents, without whom he would not have had the opportunity to perform this research.

TABLE OF CONTENTS

LIST OF FIGURES. vi

LIST OF TABLES x

ABSTRACT xi

1 OVERVIEW OF THE INTERNAL PHOTOEMISSION PROCESS IN PTSI

1 Introduction 1
2 A Brief Description of the Internal Photoemission Process. 5

2 BACKGROUND AND BASIC THEORY OF INTERNAL PHOTOEMISSION

1 Metallurgy of the Diodes 9
2 Description of the Schottky Barrier. 13
3 Derivation of the Modified Fowler Equation for Escaping Holes 20
4 Experimental Verification of the Modified Fowler Equation. 31
5 Extensions to the Modified Fowler Equation . . 40

3 THE NEW MODEL FOR INTERNAL PHOTOEMISSION

1 Development of the Model 49
2 Characteristics of the Model 59
3 Discussion of the Parameters in the Model. . . 65
The Fermi Energy 65
The Ratio of the Effective Masses. 65
The Hot-Hole/Cold-Electron Mean Free Path. . 66
The Hot-Hole/"Phonon" Mean Free Path 69
The Mean "Phonon" Energy 69
The Transmission Coefficient 70

4 OPTICAL ABSORPTION OF THE PHOTODIODES

1 Experimental Measurements. 74
2 Error Analysis of the Absorption Data. 87

5 ANALYSIS OF THE MODEL

1 Initial Optimization with Two Free Parameters per Diode. 105
2 Optimization with One Free Parameter per Diode 111

6 CONCLUSIONS AND FUTURE WORK

1 Conclusions. 127
2 Future Work. 129

REFERENCES 131

LIST OF FIGURES

Page

Figure

1. Diagram of a PtSi/Si Schottky barrier diode with read-out electronics. 4

2. Band diagram of a PtSi on p-type silicon Schottky barrier diode depicting a semi-abrupt barrier 6

3. Electron diffraction pattern of a 20 Å PtSi film on a thinned (100) Si substrate 10

4. Transmission electron micrograph showing the Moire fringes between the overlapping PtSi and Si. 12

5. Band diagram of the Schottky barrier under the condition that a) the metal and the semiconductor are infinitely far apart and not in thermal equilibrium; b) the metal and the semiconductor are in contact and in thermal equilibrium 14

6. Band diagram of the Schottky barrier showing the effects of image force lowering 16

7. The distribution of electrons in k space for a spherical Fermi surface at 0 K. 23

8. Simplified dispersion relations for holes at the Schottky barrier maximum and in the bulk metal 24

9. The escape cap for holes in k space 26

10. Modified Fowler equation plotted in the form of a Fowler plot 30

11. Block diagram of the system used for measuring the quantum efficiency of the photodiodes . . 32

12. Fowler plot of diode 4. 34

13. Activation energy plot for diode 10 38

14. Schematic diagram showing how a thermal excitation could effect the photoemission process . 42

15. An example of how the quantum-mechanical transmission coefficient might vary as a function of the energy of the hole measured from the barrier maximum 44

16. Diagram illustrating the definition of the spherical shell of emission 54

17. Fowler plot obtained using Equation 3.10 to determine the yield 60

18. The effect of L_p' on the Fowler plots obtained using Equation 3.10. 64

19. The hot-electron/cold-electron mean free path as a function of the energy of the hot-electron measured from the Fermi level 68

20. Raman spectra of Pt on Si after a 30 minute anneal at 500° C for three different thicknesses of Pt, and a bare silicon substrate. . 71

21. Diagram illustrating the definitions of R, R' and T 76

22. Frontside reflection as a function of wavelength for the diode with a 20 Å thick PtSi film . . 79

23. Frontside reflection as a function of wavelength for the diode with a 400 Å thick PtSi film. . 80

24. Backside reflection as a function of wavelength for the diode with a 20 Å thick PtSi film . . 81

25. Backside reflection as a function of wavelength for the diode with a 400 Å thick PtSi film. . 82

26. Transmission as a function of wavelength for the diode with a 20 Å thick PtSi film 83

27. Transmission as a function of wavelength for the diode with a 400 Å thick PtSi film. 84

28. Absorption as a function of wavelength for the diode with a 20 Å thick PtSi film 85

29. Absorption as a function of wavelength for the diode with a 400 Å thick PtSi film. 86

30. Diagram illustrating the definitions of R_o, T_o, R'_o, and R_1. 90

31. Frontside reflection as a function of PtSi film thickness for 3.77 μm illumination. 93

32. Similar to Figure 31 except the illumination is from the backside and Equation 4.8 is used. . 94

33. The transmission data fit using Equation 4.9. . . 95

34. Similar to Figure 31 except the measured data has been adjusted by allowing the thickness of the diodes to vary until the error function (Equation 4.10) was minimized. 99

35. Similar to Figure 34 for backside reflection. . . 100

36. Similar to Figure 34 for transmission 101

37. A comparison of the measured and calculated absorption as a function of PtSi film thickness 103

38. Similar to Figure 37 except the film thickness as determined by the optical best fits was used for the measured data. 104

39. Flow chart of the routine used to find the values of E_f, L_e, τ, L'_{pi}, and $\hbar\omega_i$ 108

40. A log-log plot of $\hbar\omega$ as a function of L'_p for the ten diodes used in the optimization routine . 109

41(a). A Fowler plot for the internal yield of diode 2 showing both the measured data and the predictions of Equation 3.10. 113

41(b). Similar to Figure 41(a) for diode 3 114

41(c). Similar to Figure 41(a) for diode 4 115

41(d). Similar to Figure 41(a) for diode 5 116

41(e). Similar to Figure 41(a) for diode 6 117

41(f). Similar to Figure 41(a) for diode 7 118

41(g). Similar to Figure 41(a) for diode 8 119

41(h). Similar to Figure 41(a) for diode 9 120

41(i). Similar to Figure 41(a) for diode 10. 121

41(j). Similar to Figure 41(a) for diode 11. 122

LIST OF TABLES

Table | page

1. Overview of the characteristics of the diodes used in this work 35

2. A comparison of the values of the thickness from the two different measurement techniques. . . 96

3. The values of n and k which best fit the reflection and absorption data tabulated as a function of the incident photon wavelength. . 102

4. The values of the parameters which are not affected by variations in processing. 124

5. The value of L_i for each of the ten diodes. . . . 126

ABSTRACT

In this work, the theory of internal photoemission is reviewed and extended for the special case of platinum silicide Schottky barrier infrared photodiodes. Vickers' model of hot-electron-mode photodetection is recast in terms of hot-holes, and the effects of carrier energy loss due to phonon collisions, as well as the depletion of the occupation of the emitting states due to emission are included.

The optical absorption of the Schottky diodes is measured and used to relate the quantum efficiency of the diodes to the internal yield as calculated from the model.

By including the effects of the carrier energy loss due to phonon collisions and the depletion of the occupation of the emitting states in the model, one can resolve previously unexplained anomalies in the photoresponse data (the shape of the Fowler plots, the absolute magnitude of the yield, and the difference between the optical and thermal barriers). Independent estimates are obtained for the mean free path between hot-hole/phonon, hot-hole/cold-electron, and hot-hole/imperfection collisions as well as the mean phonon energy, mean transmission coefficient across the Schottky barrier, and the Fermi energy.

The model is found to be in excellent agreement with the experimental data for parameter values consistent with those reported in the literature.

Some degree of correlation is found to exist between the one free variable for each diode and the processing used for that diode. Namely, the temperature of the substrate during deposition is correlated with the value of the mean free path between imperfection scattering events.

CHAPTER 1

OVERVIEW OF THE INTERNAL PHOTOEMISSION PROCESS IN PTSI

Introduction

The process by which electrons are photoemitted from a metal into a vacuum (photoemission) was of great interest at the time that the theories of the quantum nature of light, the work functions of metals, and the general nature of energy levels in solids were under intensive study. A similar process, internal photoemission, was subsequently used as a tool to measure the mean free path of electrons in metals. Internal photoemission differs from vacuum photoemission in that the carriers are emitted from the metal into a semiconductor with which it is in intimate contact, and that the carriers can be either electrons or holes[1].

More recently, internal photoemission has been used directly as a process for photodetection. In this case, the photodetector consists of a metal layer on a semiconductor substrate (a Schottky diode) with electrical contacts made to both the substrate and the metal layer. Schottky diode photodetectors suffer from low responsivity, and until recently were not widely used. However in the last few years they have emerged as a state-of-the-art infrared

detector (despite their low responsivity) due to two factors; the evolution of two dimensional multiplexers which enable large numbers of detectors to stare at a scene simultaneously, and the inability of any other infrared technology with higher responsivity to take advantage of these multiplexers. Schottky diode technology matches ideally with such multiplexers since indentical Schottky diodes can be manufactured in large numbers using the same process procedure as the multiplexer for a very low cost[2].

The theory of operation of Schottky barrier photodetectors has been addressed by several authors[3,4,5]. Their work has explained the general characteristics of the photoresponse; however, several specific features of the photoresponse have remained puzzling. In this work, the process by which platinum silicide Schottky barrier infrared photodiodes detect optical radiation is further investigated with the intent of explaining these anomalous features of the photoresponse.

The process of internal photoemission consists of three distinct parts: absorption, transport, and emission[1]. Since none of the constituent parts are independent of the others, this chapter will briefly describe the entire process, while the remaining chapters will give a detailed description of each subprocess.

The diodes used in this work consist of a thin platinum silicide (PtSi) film on a p-type silicon substrate (see Figure 1). All three interfaces are assumed to be optically flat and plane parallel. Ohmic contacts are made with both the PtSi film and the silicon substrate. Whenever infrared radiation is incident on the diode, a photocurrent is generated. The photocurrent is measured as a voltage across a load resistor, where the voltage is proportional to the incident photon flux.

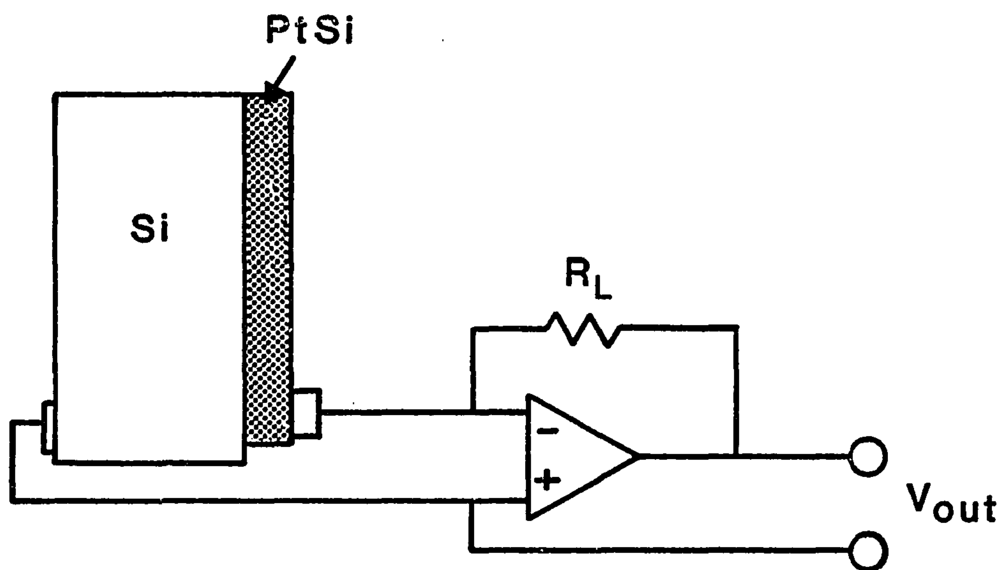

Figure 1. Diagram of a PtSi/Si Schottky barrier diode with read-out electronics.

A Brief Description of the Internal Photoemission Process

As stated in section 1, the three parts of internal photoemission are: (1) absorption, an incident photon excites an electron-hole pair in the metal; (2) transport, the hole randomly walks through the film until it reaches the Schottky barrier; (3) emission, the hole traverses the Schottky barrier from the metal into the semiconductor resulting in a current which can be measured. The precise definition of the Schottky barrier is discussed in section 2.3; however it is adequate to describe the barrier as a semi-abrupt potential maximum at the interface as shown in Figure 2.

The absorption is assumed to take place in the metal which is a good approximation for photons with energy less than 1.1 eV. (Photons of greater energy will be absorbed both in the metal and in the semiconductor, which is a complication that is not considered here.) Each photon is assumed to be reflected, transmitted, or absorbed (excites an electron-hole pair). Other absorption processes are ignored. Typically, although not necessarily, the Schottky diodes are illuminated from the silicon side (backside illumination) as shown in Figure 2. Backside illumination

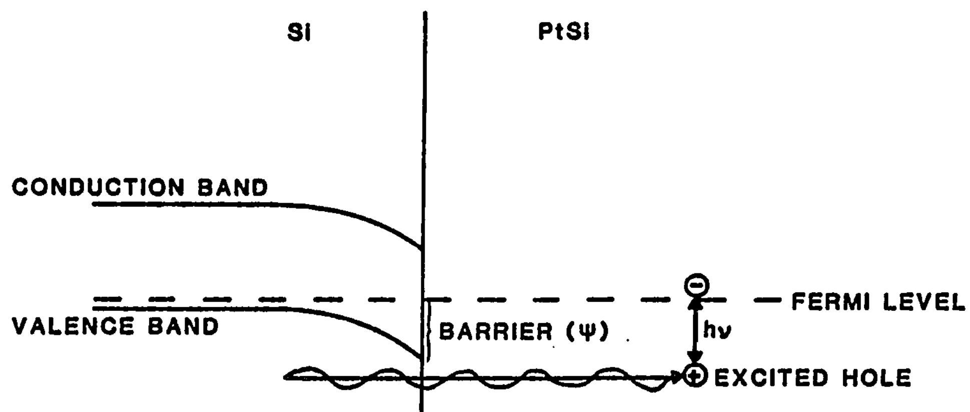

Figure 2. Band diagram of a PtSi on p-type silicon Schottky barrier diode depicting a semi-abrupt barrier.

enhances the absorption of the PtSi film since the silicon substrate acts as an index matching medium between the air and the metal. Figure 2 also shows the excited hole which can potentially traverse the barrier. Notice that the electron cannot be emitted into the semiconductor since its energy lies in the band gap of the semiconductor.

Once excited, the hole is assumed to travel ballistically through the metal until it is either thermalized or reaches the barrier for emission. The transport can involve collisions with both interfaces as well as with cold electrons and the lattice; the lattice and cold-electron collisions cause the hot-hole to lose some of its energy. After many lossy collisions the energy of the hole is reduced to the point that it can no longer escape and is in effect "thermalized". Upon each collision, the hole momentum is redirected. Bulk collisions are assumed to redirect the momentum uniformly into a sphere, while interface collisions redirect the momentum into a hemisphere.

When a hot-hole reaches the barrier it can traverse the barrier only if the conditions of conservation of energy and conservation of momentum can be met. Even if these conditions are met, there is still a finite probability that the hot-hole will be reflected, due to the quantum-mechanical nature of the potential barrier and the effects of the lattice mismatch across the barrier.

The probability that a photon incident on the photodiode will cause a hole to be emitted across the barrier is the quantum efficiency of the diode. The quantum efficiency is given by the expression

$$\eta = Y \cdot A \qquad 1.1$$

where Y is the internal yield and A is the optical absorption of the PtSi film. The internal yield is the probability that an excited hole is emitted, and the absorption is the probability that an incident photon is absorbed.

Chapter 2

BACKGROUND AND BASIC THEORY OF INTERNAL PHOTOEMISSION

Metallurgy of the Diodes

The diodes used in this experiment were manufactured by the Rome Air Development Center's Electronic Device Technology Branch at Hanscom Air Force Base. The process used to manufacture the diodes consists of electron beam evaporation of platinum onto the etched surface of a (100) Silicon wafer with resistivity greater than 1 Ω cm. The wafers were then heated to 350°C to form and anneal the PtSi film. The diodes used for the yield and activation energy measurements were 490 μm in diameter, while 1.5 cm diameter diodes from the same wafer were used for the absorption, transmission electron microscopy (TEM), and transmission electron diffraction (TED) measurements. Both sets of diodes were surrounded by implanted guard rings.

The thickness of the platinum silicide film was determined by using a quartz oscillator to monitor the mass of the deposited platinum and then calculating the thickness of the PtSi film which would have the same mass of platinum.

Figure 3 shows part of the transmission electron diffraction pattern of a 20 Å platinum silicide film on a

Figure 3. Electron diffraction pattern of a 20 Å PtSi film on a thinned (100) Si substrate.

The diffraction spots marked by (1), and (3) correspond to the 002 and 220 reflections in the PtSi respectively. The diffraction spot marked by (2) corresponds to the 220 reflection in the silicon substrate.

thinned silicon substrate. The observed diffraction pattern is identical to that reported in the literature for PtSi on (100) silicon[6]. In Figure 3 the diffraction spots from the 002 and 220 reflections of the PtSi as well as the 220 reflection of the silicon can be seen. Since the diffraction pattern from the PtSi is a localized arc which is strongly correlated with the substrate pattern rather than a diffuse circle, the PtSi is seen to be nearly epitaxial on the silicon. The separation between the Si and PtSi diffraction spots indicate that the spacing between the lattice planes in the two materials is slightly different. A comparison of the spacings of PtSi to that of Si shows that the lattice mismatch between the two is about 6% for these particular orientations.

Transmission electron microscopy was used to analyze the continuity of the films. Figure 4 shows a TEM image of the same 20 Å thick PtSi film. The fringes shown in the image are the Moire pattern which results when the interference patterns of the Si and PtSi are combined[7]. The persistence of the Moire fringes across the image indicate that the film is continuous.

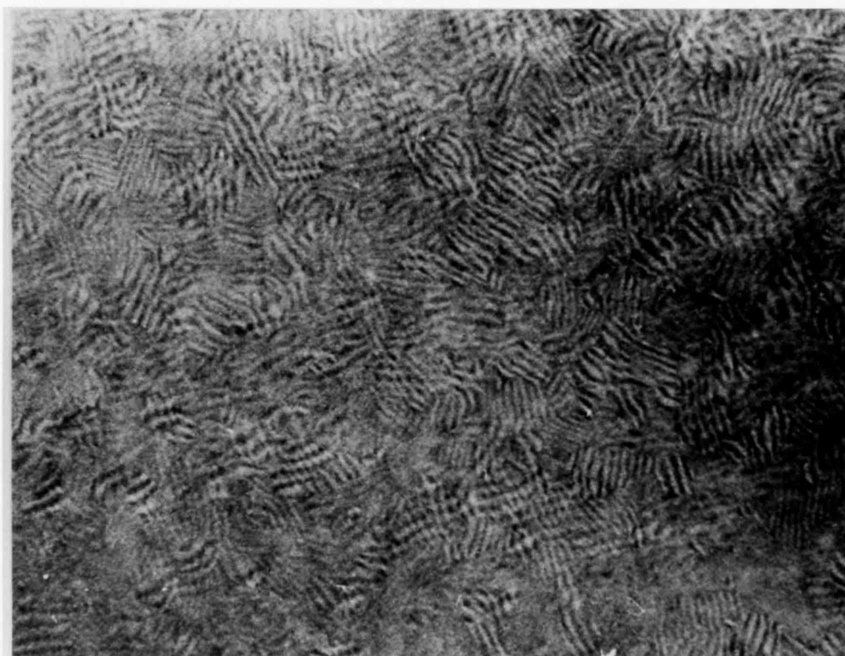

Figure 4. Transmission electron micrograph showing the Moire fringes between the overlapping PtSi and Si.

Description of the Schottky Barrier

At the interface between the PtSi and the silicon, a Schottky barrier is formed. Figure 5 illustrates two stages of formation of a hypothetical metal-semiconductor system. In Figure 5a the metal and p-type semiconductor are infinitely far apart, and not in thermal equilibrium. The height of the external photoemission barrier (work function) for the metal is Ψ_m. For the semiconductor, χ and E_g are the electron affinity and band gap respectively. As the metal and semiconductor are brought together, their Fermi levels must coincide. Figure 5b illustrates the final structure where the interface region of the semiconductor has been depleted of holes. The Fermi levels are now aligned and the energy barrier Ψ_o created. In this simple model, the height of the barrier is given by[8]

$$q\Psi_o = E_g - q(\Psi_m - \chi) \qquad 2.1$$

A more precise description of the barrier is obtained by noticing that a charge displaced from a metal slab will be acted on by an attractive image force given by

$$F = \frac{-q^2}{16\pi\epsilon_s x^2} \qquad 2.2$$

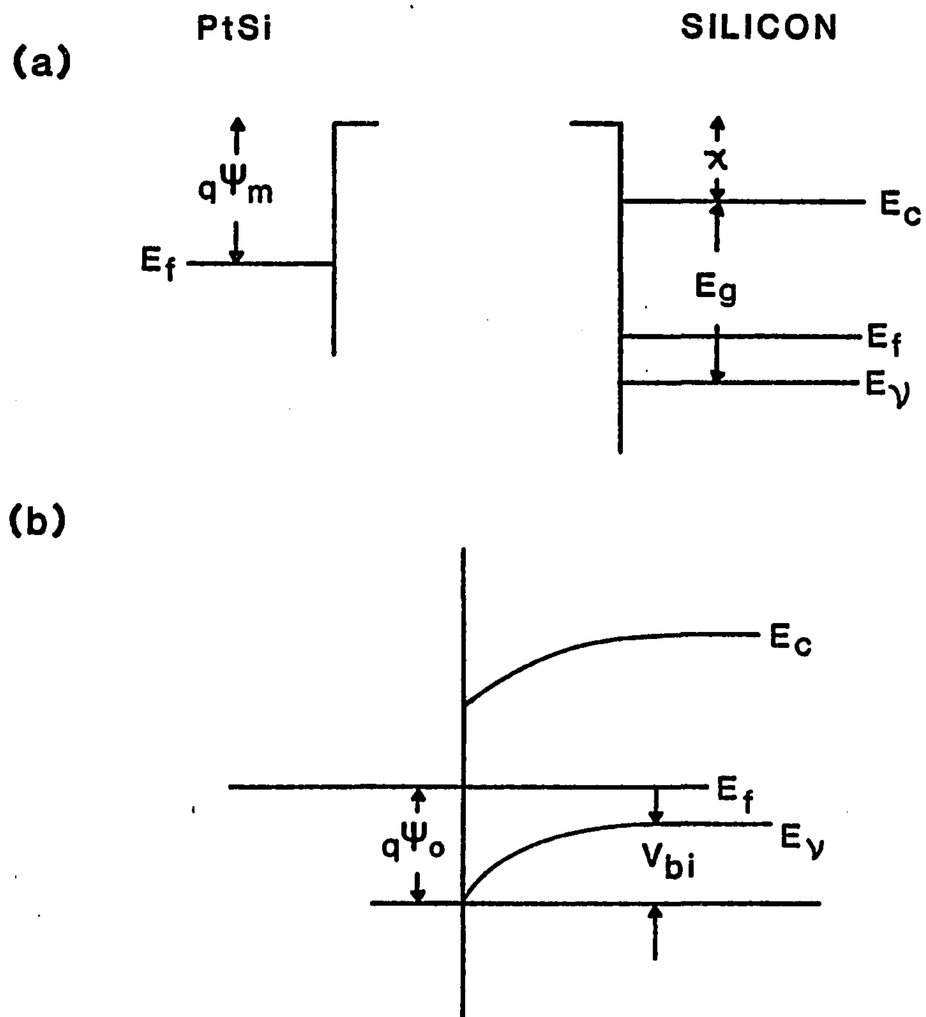

Figure 5. Band diagram of the Schottky barrier under the condition that a) the metal and the semiconductor are infinitely far apart and not in thermal equilibrium; b) the metal and the semiconductor are in contact and in thermal equilibrium.

This force combined with the potential induced by the depletion region in the semiconductor will reduce the actual barrier height. The resulting potential as a function of distance from the barrier is shown in Figure 6 and is given by

$$V(x) = q\Psi_o - \frac{q^2 N_a}{\epsilon_s}\left(Wx - \frac{x^2}{2}\right) - \frac{q^2}{16\pi\epsilon_s x} \qquad 2.3$$

where q is the elementary charge, N_a is the acceptor concentration, ϵ_s is the dielectric constant of the silicon, x is the distance into the semiconductor from the interface, and W is the depletion region depth (distance to flatband) given by

$$W = \left(\frac{2\epsilon_s}{qN_a}\left(V_{bi} + V_R\right)\right)^{1/2} \qquad 2.4$$

where V_{bi} is the built-in voltage of the interface, and V_R is the reverse bias on the diode.

The peak of the barrier is defined as the point where Equation 2.3 goes through a maximum, and is found by differentiating Equation 2.3 with respect to x and setting the derivative equal to zero. The barrier height is found to be approximately

$$q\Psi = V_{max} = q\Psi_o - \frac{q^2}{2\epsilon_s}\left(\frac{2\epsilon_s N_a (V_{bi} + V_R)}{\pi^2 q}\right)^{1/4} \qquad 2.5$$

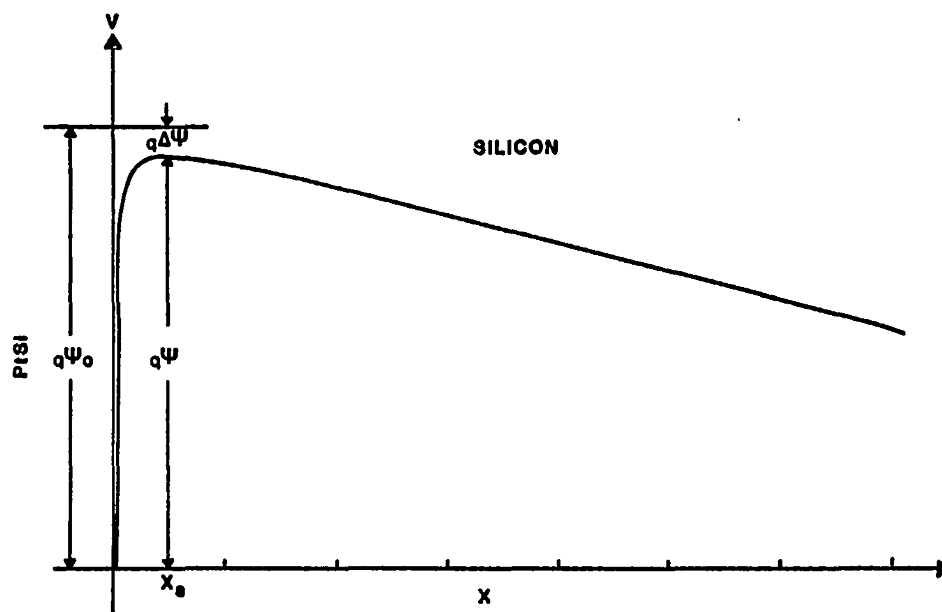

Figure 6. Band diagram of the Schottky barrier showing the effects of image force lowering.

where Ψ_o is still defined by Equation 2.1. From Equation 2.5 it can be seen that the barrier has been lowered by an amount

$$\Delta\Psi = \frac{q}{2\epsilon_s}\left(\frac{2\epsilon_s N_a (V_{bi} + V_R)}{\pi^2 q}\right)^{1/4} \qquad 2.6$$

From Equation 2.3 evaluated at the maximum one finds that the barrier shift from the interface (x_s) is given by.

$$x_s = \frac{1}{4}\left(\frac{q}{\pi^2 2\epsilon_s N_a (V_{bi} + V_R)}\right)^{1/4} \qquad 2.7$$

For a reverse biased diode with typical dopant concentration, x_s is on the order of 48 Å.

From the preceding discussion it is clear that the location of the barrier is rather ambiguous. Arguments can be made for its location being at the physical interface, or the potential maximum. In an effort to eliminate the ambiguity, the barrier is defined as the point where a hot-hole is most likely to be reflected. Hot-holes with energy insufficient to escape are reflected at the point at which the barrier potential exceeds the energy of the hole. From Figure 6 it can be seen that for a uniform distribution of hole energies, the most probable point for the barrier to exceed the hole energy is at the point the potential function (Equation 2.3) has steepest slope, this point is at the

interface. Hence, the most likely point of reflection for holes with energy less than the barrier is at the interface. Very few of the hot-holes are reflected at the potential maximum, since at the maximum, the slope of the potential function is zero. Hence following this definition of the "barrier", it is assumed that the location of the barrier is at the interface.

One of the interesting features of the Schottky barrier devices is that the height of the barrier can be controlled. From Equation 2.6, one can see that an increase in the dopant concentration of the semiconductor or in the reverse bias on the diode lowers the barrier. Since the spectral region over which the diode responds is a function of the barrier height, one can tailor a diode's performance for a specific application by changing the dopant concentration.

There are two drawbacks to lowering the barrier by this method. First, the number of thermally generated holes which can surmount the barrier will increase, necessitating further cooling of the diode. Second, the increased doping or voltage will not only lower the barrier but make it narrower as well. The narrow barrier will be much more susceptible to tunneling which cannot be rectified by further cooling. For diodes with significantly thinned barriers, the tunneling current will dominate the conduction

process and make the diode behave more like an ohmic contact.

Derivation of the Modified Fowler Equation for Escaping Holes

With the barrier and the system in general adequately described, a detailed description of the photoemission process can be obtained. An exact model for the photoemission process would include a description of the band structure of the PtSi film and the silicon substrate as well as how the two are related near the interface. Little is known of the band structure of PtSi, and even less is known about how PtSi and silicon are related at the interface. In an effort to make the photoemission model tractable while maintaining insight into the physical processes involved, several simplifying assumptions are made:

1) PtSi is assumed to be an ideal metal, with the dispersion relation:

$$E = \frac{(\hbar k)^2}{2m_m} \qquad 2.8$$

where $\hbar k$ is the hole momentum, m_m is the effective mass of the hole, and E is the energy of the hole as measured from the bottom of the conduction band.

2) The probability of exciting an electron-hole pair is independent of the initial and final states of the transition.

3) The rate of thermalization is fast compared to that of photon emission, i.e. the excited hole will lose its energy to collisions with the lattice and cold electrons before it has a chance to reemit a photon.

4) The detector is operated at 0 K. This assumption is incorporated to eliminate the "thermal tail" of Fermi-Dirac statistics. Section 2.5 shows how the thermal effects should be incorporated; however since the Schottky diodes are generally cooled to liquid nitrogen temperatures, the thermal tail is negligible.

5) The energy of the absorbed photon ($h\nu$) is less than the Fermi energy (E_f) as is generally the case in the infrared.

6) The holes are assumed to travel ballistically.

7) The PtSi/Si interface is characterized by the barrier as described in section 2.2.

The complete model for the internal yield includes the effects of the excited hole (hot-hole) colliding with both interfaces as well as any of the bulk scattering sites, and will be developed in chapter 3. At this point, a model neglecting collisions similar to that developed by Fowler[3] as modified by Vilms, Cohen and Archer[9] is presented (the

only difference being that their model was developed for escaping electrons).

Figure 7 depicts a distribution of electrons in momentum space in the PtSi film. The fourth assumption implies that the electrons fill all states within the outer circle (sphere), and no states outside that circle. Only electrons which have crystal momentum within the range

$$(2m_m(E_f - h\nu))^{1/2} < \hbar k < (2m_m E_f)^{1/2} \qquad 2.9$$

can be excited by an incident photon of energy $h\nu$, since only these states have an occupied initial state and an unoccupied final state. These initial states are shown in the figure as the spherical shell of excitation.

When a photon is absorbed, an electron-hole pair is generated in the metal film. For the case of PtSi on p-type silicon, the hole can escape into the semiconductor if it has sufficient momentum directed normal to the barrier, and the momentum directed parallel to the barrier and the total energy can be conserved.

Simplified dispersion relations for the holes at the Schottky barrier and in the bulk metal are shown in Figure 8. From the figure, the condition for conservation of total energy for holes is found to be

$$-\frac{\hbar^2 k_\perp^2}{2m_m} - \frac{\hbar^2 k_\parallel^2}{2m_m} = -E_f + \Psi + \frac{\hbar^2 k_\perp'^2}{2m_s} + \frac{\hbar^2 k_\parallel'^2}{2m_s} \qquad 2.10$$

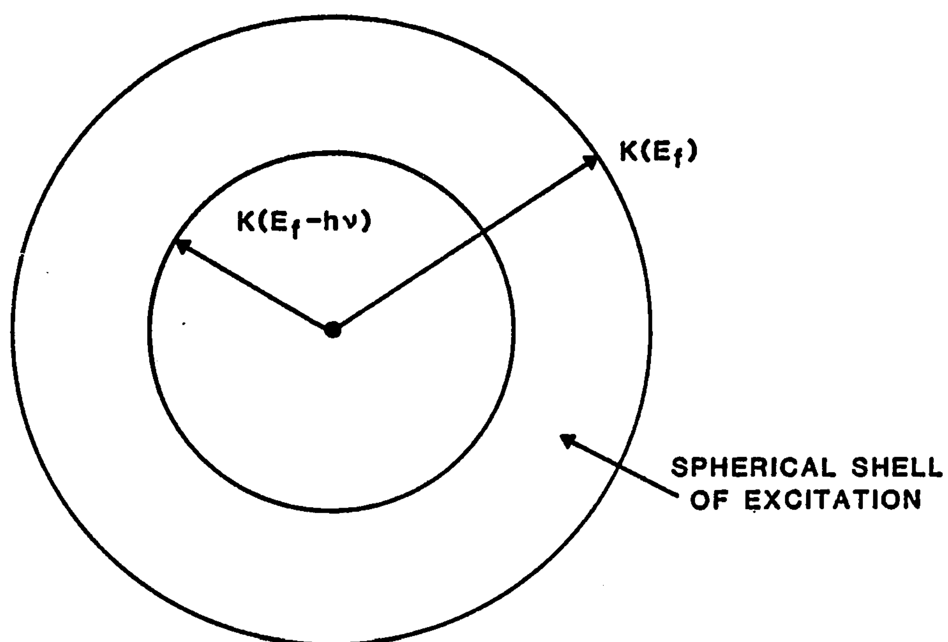

Figure 7. The distribution of electrons in k space for a spherical Fermi surface at 0 K.

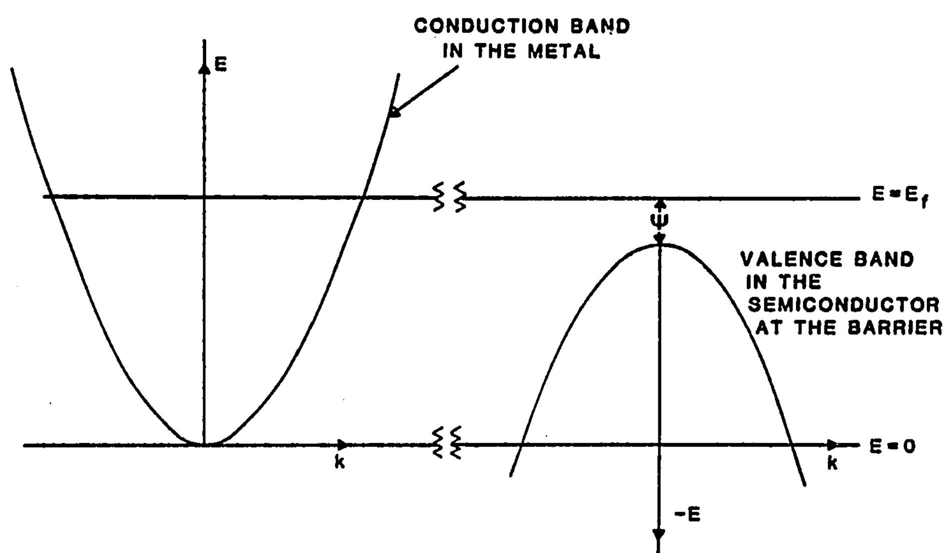

Figure 8. Simplified dispersion relations for holes at the Schottky barrier maximum and in the bulk metal.

Here m_s and m_m are the effective masses in the silicon substrate and the metal film (PtSi film) respectively, $k_\perp$ and $k_\parallel$ are the magnitude of the perpendicular and the parallel part of the hole's wave vector in the platinum silicide, and $k'_\perp$ and $k'_\parallel$ are the corresponding values in the silicon substrate. Imposing the conditions that the final kinetic energy directed normal to the barrier must be greater than zero and that parallel momentum is conserved ($k_\parallel = k'_\parallel$), one obtains

$$\frac{\hbar^2 k_\perp^2}{2m_m} + \frac{\hbar^2}{2}\left(\frac{1}{m_m} + \frac{1}{m_s}\right)k_\parallel^2 \leq E_f - \Psi \qquad 2.11$$

Here the equality is satisfied for an ellipsoid of revolution in k space. If electrons were the emitted carriers and their mass was the same in the metal and the semiconductor, then the term for electron emission corresponding to the one in parentheses (with a sign change in one term) would become zero, and the condition for emission would simply be that the normal component of the carrier's kinetic energy is greater than the barrier. However for hole emission, the conservation of parallel momentum is always explicitly represented in the condition for emission.

Since only states in the spherical shell of excitation are excited, the states which will emit are shown as a hatched region in Figure 9. The hatched region is known

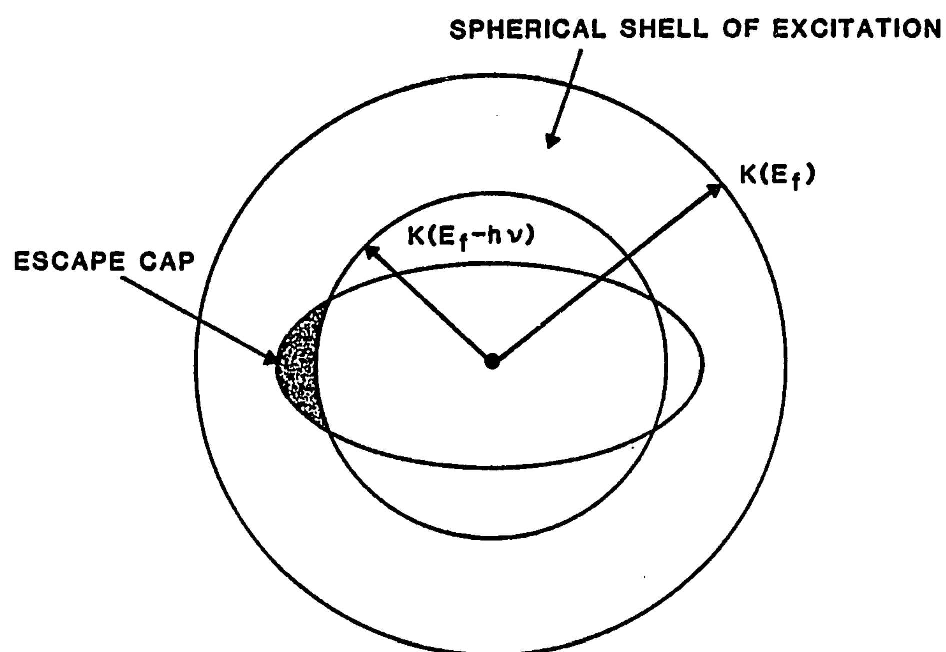

Figure 9. The escape cap for holes in k space.

The hatched region on the left corresponds to holes which may escape over a barrier on the right.

as the escape cap. The states in the escape cap are assumed to have unity probability of escape which is strictly true only in the absence of quantum mechanical reflections at the barrier.

The volume of the cap is given by

$$V_c = \int_0^{2\pi} \int_{k(E_f - h\nu)}^{k(E_f - \Psi)} \int_0^{\Theta(k)} k^2 \sin\Theta \, d\Theta \, dk \, d\phi \qquad 2.12$$

The angle $\Theta(k)$ is defined as the angle the momentum vector of the hot-hole momentum has with respect to a vector directed normal to the interface, and is given by

$$\Theta(k) = \sin^{-1}\left(\frac{k_{\parallel}}{k}\right) \qquad 2.13$$

Using the fact that

$$k^2 = k_{\perp}^2 + k_{\parallel}^2 \qquad 2.14$$

and Equation 2.11 to solve for $k_{\parallel}$ in terms of k, $\Theta(k)$ is found to be

$$\Theta(k) = \sin^{-1}\left(\frac{[(2m_s/\hbar^2)(E_f - \Psi) - (m_s/m_m)k^2]^{1/2}}{k}\right) \qquad 2.15$$

By integrating Equation 2.12 and defining M to be the ratio of the effective mass in the semiconductor to that in the metal film, one finds the volume of the cap to be

$$V_c = \frac{2\pi}{3}\left(\frac{2m_m}{\hbar^2}\right)^{\frac{3}{2}} \frac{M(E_f - \Psi)^{\frac{3}{2}}}{(1 + M)}$$

$$+ \frac{(E_f - (1 + M)h\nu + M\Psi)^{\frac{3}{2}}}{(1 + M)} - (E_f - h\nu)^{3/2} \qquad 2.16$$

The yield is obtained by dividing the volume of the cap by the volume of the spherical shell of excitation, and is given by

$$Y_F =$$

$$\frac{M(E_f - \Psi)^{\frac{3}{2}} + (E_f - (1 + M)h\nu + M\Psi)^{\frac{3}{2}} - (1 + M)(E_f - h\nu)^{\frac{3}{2}}}{2(E_f^{3/2} - (E_f - h\nu)^{3/2})(1 + M)}$$

2.17

In the limit that $E_f >> h\nu > \Psi$ the yield is approximately

$$Y_F \simeq M^{1/2} \frac{(h\nu - \Psi)^2}{8E_f h\nu} \qquad 2.18$$

Equation 2.18 is known as the modified Fowler equation, and to this order of approximation is the same for either escaping electrons or holes. Multiplying Equation 2.18 through by $h\nu$ and taking the square root of both sides, one obtains

$$\sqrt{Y_F h\nu} \simeq \sqrt{M^{1/2}/8E_f} \quad (h\nu - \Psi) \qquad 2.19$$

which is linear in $h\nu$. When $\sqrt{Y_F h\nu}$ is plotted as a function of photon energy the intercept of the function with the abscissa is the barrier height (see Figure 10). Due to the linearity of the function and ease of determining the barrier height, quantum efficiency data for Schottky diodes is generally presented in this form (Fowler plot).

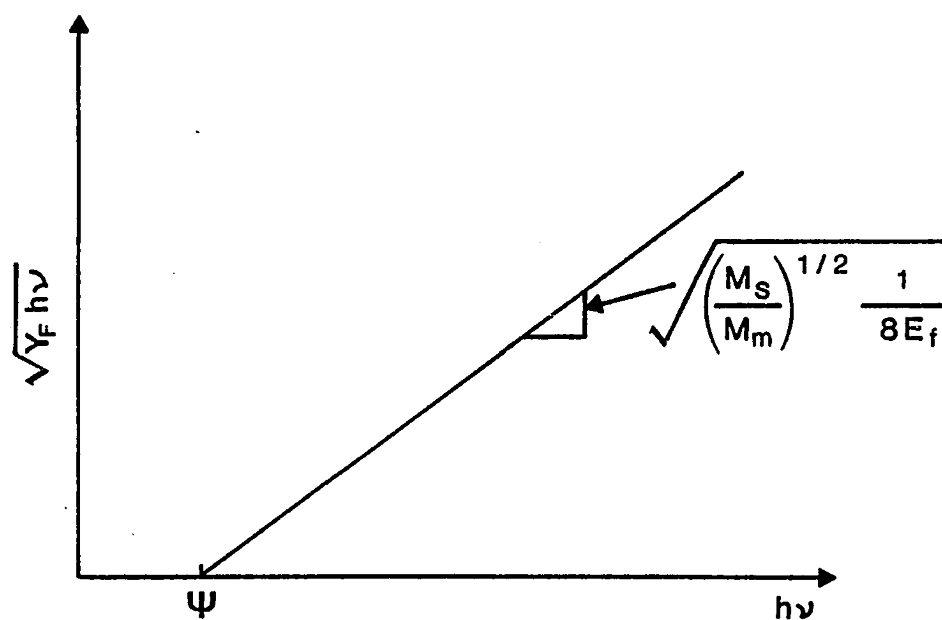

Figure 10. Modified Fowler equation plotted in the form of a Fowler plot.

Experimental Verification of the Modified Fowler Equation

In order to evaluate the validity of the modified Fowler equation, the quantum efficiency was measured as a function of wavelength and compared to the predictions of the equation. The quantum efficiency of the photodiodes was measured using the system illustrated in Figure 11. A globar illuminated the entrance slit of a Perkin-Elmer model 98 monochromator. The exit slit was imaged onto the photodiode which was mounted on the cold finger of a Displex refrigeration system. All of the yield measurements were taken with the photodiode at 40 K. The radiation at the entrance slit was chopped at 135 hz while the signal from the photodiode was read out by a PAR model 124 A lock-in amplifier. The entrance slit of the monochromator was covered with a room temperature silicon wafer to block any stray radiation which might be absorbed in the silicon. The lock-in amplifier and the stepper motor for the monochromator were both interfaced to an HP 9826 computer which coordinated the measurements and recorded the data.

Absolute calibration of the system was performed using a Laser Precision pyroelectric detector which was limited by an aperture of the same size as the diodes being

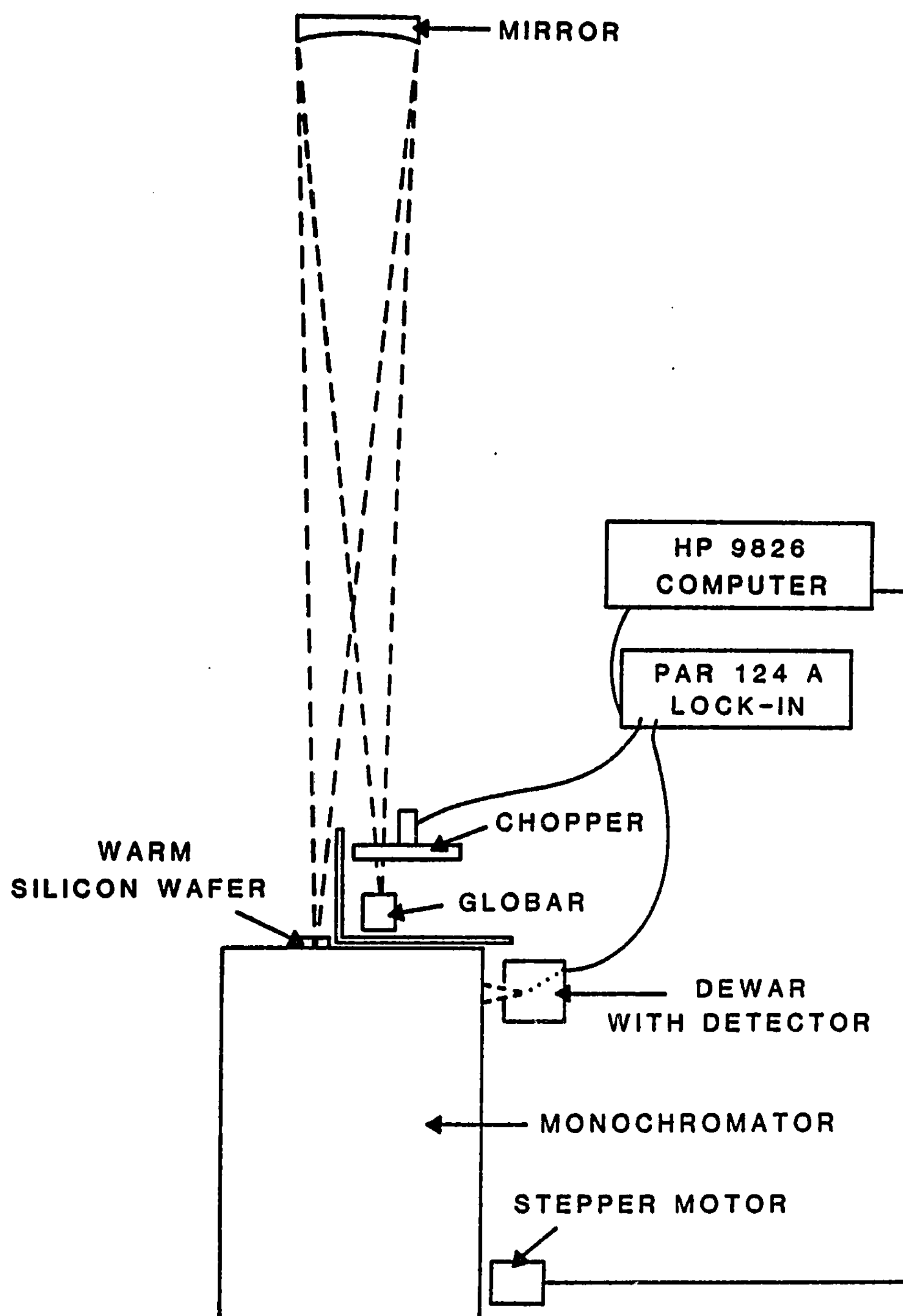

Figure 11. Block diagram of the system used for measuring the quantum efficiency of the photodiodes.

tested. The pyroelectric detector was calibrated by illuminating it directly with a blackbody source and calculating the responsivity from the measured pyroelectric signal and known incident irradiance. The feedback resistor for the pyroelectric was 10^{11} Ω which gave a uniform gain for electrical frequencies in the neighborhood of 135 hz.

Eleven diodes were used in this experiment ranging in thickness from 5 to 400 Å of PtSi. Table 1 lists the diodes and their thicknesses. The quantum efficiencies for the diodes ranged in value from 8% at 1.28 μm down to 0.004% at 6.0 μm. The quantum efficiency of each diode at 1.46 μm is also recorded in Table 1. The variation in the quantum efficiency from diode to diode is explained in chapter 5; however a trend of higher yields for thinner films is vaguely evident. All diodes were measured with an applied reverse bias of one volt. The data from the quantum efficiency measurements combined with the data from the absorption measurements is presented in more detail in chapter 5.

A diagram of the measured quantum efficiency of a Schottky barrier diode as a function of the incident photon energy for a typical diode is shown in Figure 12. The data are plotted in the form of a Fowler plot as discussed in section 2.3. Superimposed on the data points is a fit of the linear region of the curve. From Figure 12 it can be seen that the linear fit does a reasonably good job of

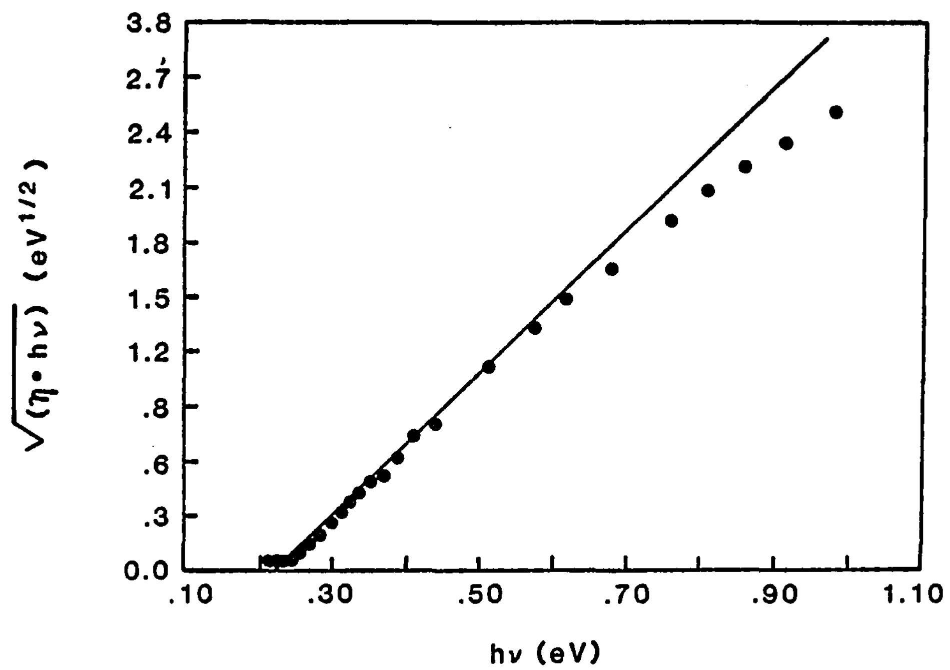

Figure 12. Fowler plot of diode 4.

Table 1. Overview of the characteristics of the diodes used in this work.

Diode Number	Thickness (Å)	Quantum Efficiency (%)	Ψ_{op} (eV)	Ψ_{th} (eV)
1	5	6.9	0.228	0.206
2	10	3.4	0.223	0.186
3	20	2.0	0.252	0.181
4	20	5.7	0.222	0.195
5	40	4.1	0.238	0.193
6	80	2.5	0.247	0.203
7	100	5.2	0.217	0.167
8	100	4.2	0.232	0.202
9	120	1.8	0.251	0.215
10	200	2.8	0.240	0.207
11	400	2.6	0.247	0.210

fitting the data as predicted in section 2.3. However for photon energies near 1 eV the measured data fall away from linear, and for photon energies near the barrier the Fowler yield is greater than expected. The slope of the linear fit is 4.1 $eV^{-(1/2)}$ corresponding to a value of 7.4 meV for E_f, which is considerably lower than expected in comparison to the values for other materials in the literature[10], and is too low for the assumptions used in deriving Equation 2.17.

The intercept of the line fitted to the linear region with the abscissa in Figure 12 is the optical barrier height of the diode (Ψ_{op}). In Figure 12 the barrier height is shown to be 0.222 eV., while Table 1 has the optical barrier heights for all eleven diodes listed.

Another method for measuring the Schottky barrier height of a diode is to use an activation energy measurement. In this technique the dark current is measured as a function of temperature at a fixed reverse bias. From the diode equation, the current as a function of reverse bias is given by[8]

$$I_R = -AA^{**}T^2 \exp\left(-\frac{q\Psi}{kT}\right)\left(\exp\left(-\frac{qV_R}{kT}\right) - 1\right) \qquad 2.20$$

where A is the active area of the diode, A^{**} is the effective Richardson constant, and V_R and I_R are the reverse bias voltage and current respectively. It can be seen that for a

large enough reverse bias (V_R > 40mV) the term in the second set of parentheses can be neglected. Taking the natural logarithm and rearranging terms one obtains

$$\ln(I_R/AT^2) = -\frac{q\Psi}{kT} + \ln(A^{**}) \qquad 2.21$$

Over limited temperature ranges if $\ln(I_R/AT^2)$ is plotted as a function of 1/T, the barrier height of the diode can be determined from the slope of the resulting line. Figure 13 shows an activation energy plot for diode 10. The barrier height obtained from this method is referred to as the thermal barrier. The thermal barrier heights for all of the diodes were measured at one volt reverse bias over a temperature range of 40 to 200 K. Again the Displex refrigeration system was used to control the temperature. Thermal barriers (Ψ_{th}) for the eleven diodes are listed in Table 1. As can be seen from Table 1, the barrier height measured optically is always greater than that measured using activation energy. The mean difference is 0.04 eV with a standard deviation of 0.01 eV.

At this point four discrepancies exist between the experimental data and the simple model.

1) Yields which are higher than the simple model predicts without the imposition of a very low value on E_f.
2) Roll off from linearity for high photon energies.

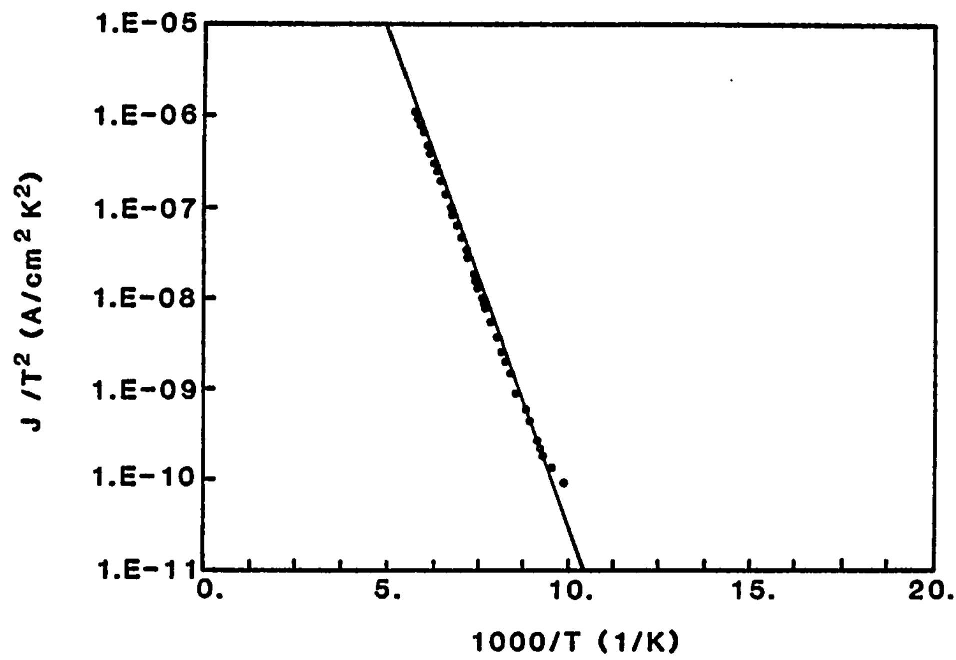

Figure 13. Activation energy plot for diode 10.

3) Finite yield for photon energies below the optical barrier.

4) A systematic discrepancy between the optical and thermal barriers.

Extensions to the Modified Fowler Equation

In this section several extensions to the modified Fowler equation are introduced in order to explain some of the anomalous effects mentioned in the previous section. The first two are introduced primarily for completeness, since they are not utilized in the model developed in the latter chapters. However each of these extensions should be considered in a complete description of the internal photo-emission process, even though their consequences are not great.

Two models exist for explaining the finite photo-yield for photon energies below the optical barrier height. The first was developed by Fowler[3] and was later modified by Vickers[5], and is based on assumptions similar to those made in section 3; however it is not assumed that the temperature is at 0 K so the "thermal tail" of Fermi-Dirac statistics must be incorporated. The expressions derived by Vickers[5] are:

for $h\nu \geq \Psi$

$$Y_F(T) = \frac{M^{1/2}}{4E_f h\nu}\left(\frac{(h\nu - \Psi)^2}{2} + (kT)^2\left\{\frac{\pi^2}{6} + \sum_{i=1}\frac{1}{i^2}\left[-\exp\left[-\frac{(h\nu - \Psi)}{kT}\right]\right]^i\right\}\right) \quad 2.22$$

and for $h\nu \leq \Psi$

$$Y_F(T) = -\frac{M^{1/2}(kT)^2}{4h\nu}\sum_{i=1}\frac{1}{i^2}\left[-\exp\frac{(h\nu - \Psi)}{kT}\right]^i \quad 2.23$$

In terms of the model from section 2.3, electrons are thermally excited above the Fermi surface leaving holes which can act as the unoccupied states for a future photoabsorption event (see Figure 14). During photoabsorption, an electron can be excited to the state left unoccupied by the thermal excitation resulting in a hot-hole in the initial state of the photoexcited electron. In this case the excitation energy is acquired by the hot-hole from both the thermal excitation and the photon. For emission, the sum of the two excitation energies must be greater than the barrier height. Equations 2.22 and 2.23 imply that the yield for photon energies of the same order as the barrier height will be greater than that predicted by the model developed in section 3, and that for photon energies slightly less than the barrier the yield will be non-zero.

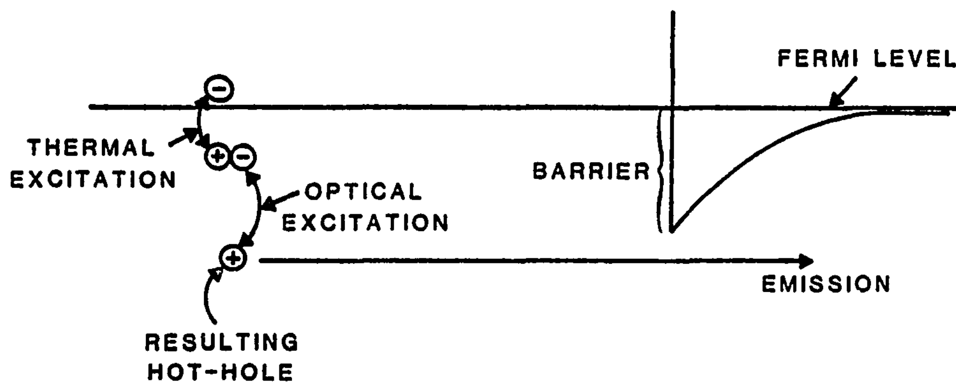

Figure 14. Schematic diagram showing how a thermal excitation could effect the photoemission process.

The second model includes the quantum mechanical nature of the potentially emitted carrier on the emission process.[12,13]. Because of the wave nature of the carrier, the probability of its escape remains finite even if its energy is below the barrier. Figure 15 shows an example of the transmission coefficient as a function of energy in excess of the barrier as calculated by Anderson et. al.[14]. The diagram shows that carriers with energies much greater than the barrier have a transmission probability of near unity. Those with energies only slightly greater than the barrier will have significantly reduced transmission probability, while electrons with energies slightly less than the barrier maintain a finite transmission probability.

The actual transmission coefficient depends not only on the energy difference between the excited hole and the barrier, but also the shape and thickness of the barrier, as well as the change in effective mass across the barrier. A smooth narrow potential function with no change in effective mass from one side to the other side will have the lowest reflection coefficient, while a wide potential function with sharp features and a large change in effective mass will have the highest reflection coefficient. Both the thermal and quantum-mechanical models are possible explanations for the enhanced yield for low photon energies. However neither model is able to explain the yields which are too large

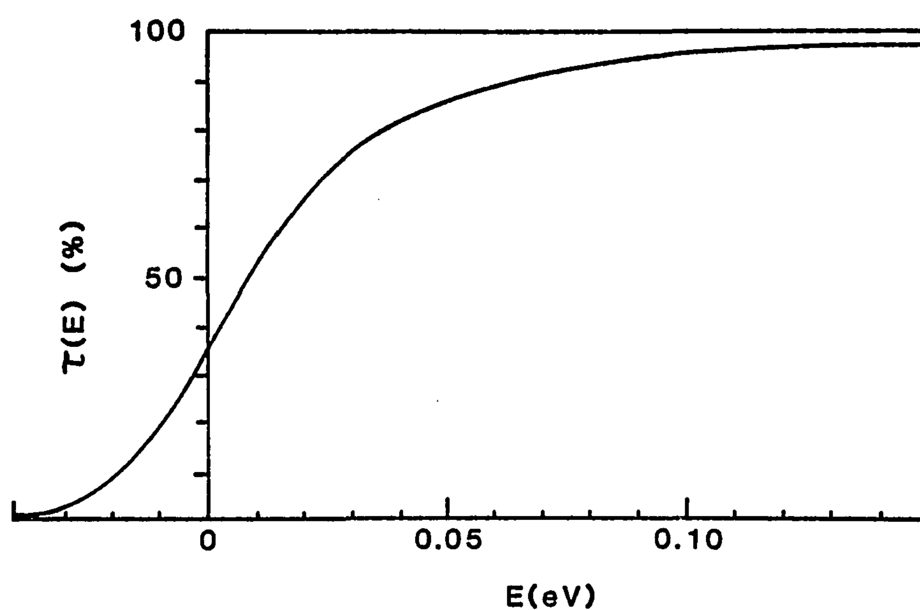

Figure 15. An example of how the quantum-mechanical transmission coefficient might vary as a function of the energy of the hole measured from the barrier maximum.

Taken from reference 14.

to be consistent with reasonable values of E_f, the roll off at high photon energies, or the discrepancy between the optical and thermal barriers.

The discrepancy between the measured value of the slope of the linear region and that expected from reasonable values of E_f has been addressed by both Dalal[4] and Vickers[5]. Both Dalal and Vickers show that the modified Fowler yield is enhanced by the effects of phonon and wall scattering which can redirect the hot-hole momentum so that it falls in the escape cap. The two models differ in that Dalal's is a one dimensional model in which the exponential decay of the density of carriers in the film due to the nonuniform optical absorption is considered. Vickers' model is three dimensional, but uniform photoabsorption is assumed. Further analysis concentrates on Vickers' model, since Vickers' model incorporates the three dimensional nature of the scattering process, and over the range of film thickness considered (5 - 400 Å) it is reasonable to assume that the absorption is uniform.

Vickers shows that the modified Fowler yield is altered by the effects of different scattering mechanisms in the PtSi film. His expression for the yield is

$$Y_V = \frac{M^{1/2}(h\nu - \psi)^2}{8E_f h\nu} \; \frac{L_e}{d} \; U(d/L^*) \qquad 2.24$$

where d is the thickness of the PtSi film, L_e is the mean free path between collisions with cold electrons and L^* is defined by

$$\frac{1}{L^*} = \frac{1}{L_e} + \frac{1}{L_p'} \qquad 2.25$$

where L_p' is the mean free path between semi-elastic collisions. $U(d/L^*)$ is defined by an expression involving well-known exponential integrals which physically represent probabilities of having no bulk collisions in the course of multiple traversals from wall to wall averaged over distance and angular parameters[5].

Vickers' result is obviously a low yield approximation since it is unbounded as L_e increases; however it does explain the high yield without imposing unrealistically low values on E_f. From equation 2.24, it can be seen that virtually any value of slope for the modified Fowler equation can be obtained by choosing the appropriate value of L_e.

In the literature it has been shown that L_e has approximately an inverse-squared relationship with the carrier energy measured from the Fermi level (See section 3.3 for further discussion). This decrease in L_e as a function of carrier energy has been proposed as an explanation for the deviation from a linear plot at high photon energies.

From equation 2.24, it can be seen that for $L_p' << L_e$ any decrease in L_e will result in a decrease in the yield. Since L_e decreases for higher photon energies, the yield will be diminished at the higher energies, which is consistent with the roll off from linearity for the high photon energies.

It should also be pointed out that the earlier comparison of the modified Fowler equation to the experimental data involved a comparison of measured quantum efficiency data to calculated internal yield data. An accurate comparison would have divided out the effects of optical absorption. In the literature it is usually assumed that the absorption is spectrally uniform over the wavelength region of interest and can be treated as a constant scale factor; however in chapter 4, it will be shown that the absorption is not spectrally uniform in this case, and that it can impact the shape of the resulting Fowler plot. Chapter 5 will include these effects in the Fowler plot analysis.

It has been shown that three of the four discrepancies between the experimental data and the simple model listed in section 2.4 can be explained by fine tuning the modified Fowler equation. The final discrepancy to be explained is the difference between the optical and the thermal barriers. The next chapter will address this final

discrepancy, and in doing so explain all four of the discrepancies with one rather simple model.

Chapter 3

THE NEW MODEL FOR INTERNAL PHOTOEMISSION

Development of the Model

As was stated in the previous chapter, Vickers incorporated scattering into the modified Fowler equation in order to explain the excess yield. In this chapter, the extensions to Vickers' model due to Mooney and Silverman[15] are incorporated into his model in the course of outlining its derivation. The extensions include treating the energy lost by the carrier during phonon creation and taking into account the fact that the population of excited states is depleted whenever carriers are emitted.

The scattering mechanisms to be included can be broken into three groups.

1) Interface scatter: An interface scatter occurs when a hot-hole interacts with either a backwall or a front wall and is not emitted. Interfaces are assumed to behave as lambertian reflectors. However the reflection need only be lambertian to the extent that the states in the spherical shell of excitation replenish the states in the escape cap.

2) Hot-hole/cold-electron scatter: This scattering mechanism is characterized by a mean free path L_e and by the fact that one scatter of this type will reduce the energy of the hole to the point that it can no longer traverse the barrier.

3) Hot-hole/"phonon" scatter: This scattering mechanism includes all bulk collisions which do not involve cold electrons (i.e. collisions with phonons, grain boundaries, lattice defects, etc.), and is characterized by a mean free path L_p' and a mean energy loss $\hbar\omega$. These collisions are assumed to redirect the momentum of the hot-hole into a sphere; however, as was the case with interface scatters, the redistribution need only replenish the states in the escape cap which have emitted.

If an excited hole is initially in the escape cap and is a distance z from the barrier, then its probability of reaching the barrier without colliding in the bulk is

$$\exp\left(-\left(\frac{1}{L_e} + \frac{1}{L_p'}\right)z\right) = e^{(-z/L^*)} \qquad 3.1$$

Integrating Equation 3.1 over the thickness of the film and normalizing, one finds the accumulated probability for escape without scatter to be

$$\alpha = \frac{1}{d}\int_0^d e^{(-z/L^*)}\,dz = \frac{L^*}{d}\left[1 - e^{(-d/L^*)}\right] \qquad 3.2$$

Here the assumption that the excitation energy is much less than the Fermi energy has been used. This assumption implies that all states in the escape cap have momentum directed approximately normal to the barrier. Also implicit in Equation 3.2 is the assumption of uniform carrier creation with distance (photoabsorption).

The holes which are not initially in the escape cap have an accumulated probability of reaching one of the interfaces equal to where

$$\beta = \frac{1}{d}\int_0^d \int_0^{\pi/2} \exp(-(d - z)/(L^*\cos\theta))\ \sin\theta\ d\theta\ dz \qquad 3.3$$

In order to include the effects of multiple reflections off the interfaces, one also defines

$$\delta = \int_0^{\pi/2} \exp(-d/L^*\cos\theta))\ \sin\theta\ d\theta \qquad 3.4$$

which is the probability that a hole which is diffusely scattered off one surface reaches the other surface without a collision.

At this point the accumulated probability that a hot-hole will be emitted without colliding in the bulk can be calculated. The probability that a hot-hole reaches the

Schottky barrier prior to colliding in the bulk (Y_{io}) is calculated by taking the sum of an infinite number of terms, where the different terms include the effects of the multiple scatters off of the interfaces. Y_{io} is given by

$$Y_{io} = Y_F \alpha + Y_F \beta e^{(-d/L^*)} \left[1 + \left(1 - \frac{2Y_F}{Y_\infty}\right)\delta + \left(1 - \frac{2Y_F}{Y_\infty}\right)\delta^2 + \left(1 - \frac{2Y_F}{Y_\infty}\right)^2 \delta^3 + \left(1 - \frac{2Y_F}{Y_\infty}\right)^2 \delta^4 + \cdots \right] \quad 3.5$$

The first term on the right is the probability that a hot-hole is initially in the escape cap and that it is able to reach the barrier. The first term (unity) in the square brackets generates the probability that the hot-hole is initially directed toward the metal/air interface, is scattered into the escape cap at the interface and is able to reach the barrier. The remaining terms in the square brackets compute the capture probabilities of hot-holes which have two or more scatters at the interfaces with alternating terms considering holes which were initially directed toward the front or the back interface.

The term $(1 - 2Y_F/Y_\infty)$ is the probability that a hot-hole is not initially in the escape cap. It may also be viewed as a counting loss correction term which is raised to the appropriate power in Equation 3.5 to reflect the number of times the carrier is scattered back from the barrier

before ultimate capture. The yield and hence this probability has been normalized to include only the states which can potentially emit. The probability that a state can potentially emit is given by the volume of the spherical shell of states which potentially emit divided by the volume of the spherical shell of excitation (see Figure 16), and is given by

$$Y_{\infty} = \frac{(E_f - \psi)^{3/2} - (E_f - h\nu)^{3/2}}{E_f^{3/2} - (E_f - h\nu)^{3/2}} \simeq \frac{h\nu - \psi}{h\nu} \qquad 3.6$$

The normalization is necessary since only a portion of the excited states can potentially emit, and the population of the states which can emit is depleted, while the population of the nonemitting states remains statistically unchanged.

Equation 3.5 can be reduced to

$$Y_{io} = Y_F\left[\alpha + \beta e^{(-d/L^*)} \frac{(1 + (1 - 2Y_F/Y_{\infty})\delta)}{(1 - (1 - 2Y_F/Y_{\infty})\delta^2)}\right] \qquad 3.7$$

In the limit that the probability of traversing the metal film becomes unity, Y_{io} approaches Y_{∞}, the maximum yield possible.

After the hot-hole reaches the barrier there is a finite probability that it will be reflected at the barrier even though it is in the escape cap. If the probability that a hot-hole in the escape cap is transmitted across the

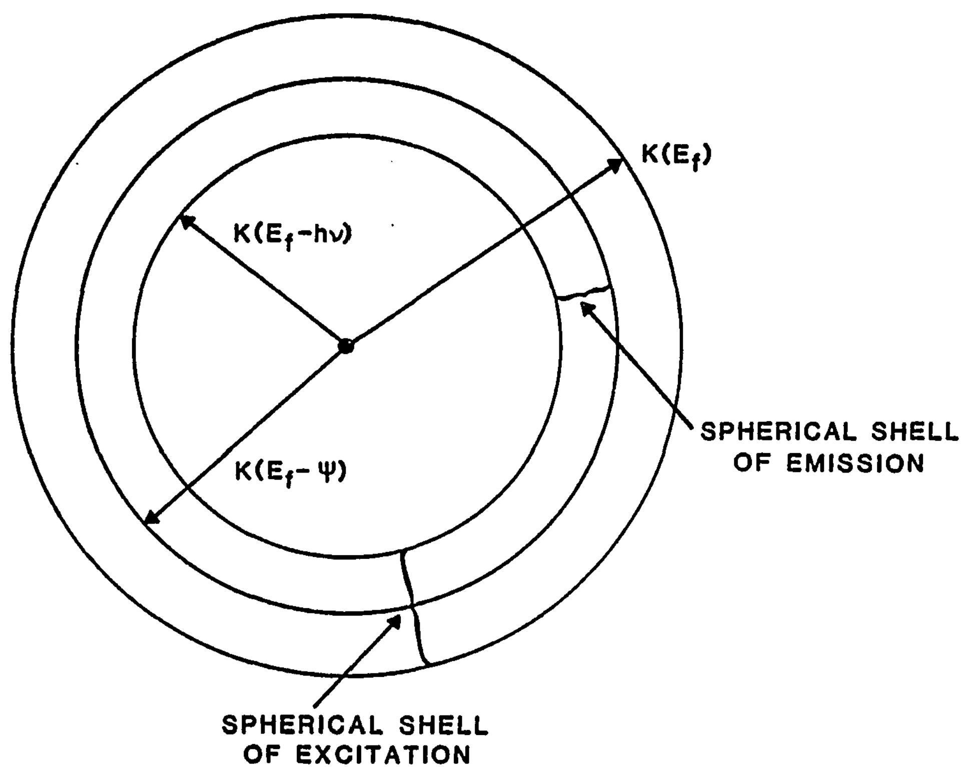

Figure 16. Diagram illustrating the definition of the spherical shell of emission.

barrier is τ, then the total yield for no collisions in the bulk is given by

$$Y_0 = Y_{io}\tau \Bigg\{ 1$$

$$+ \left[(1 - \tau)\delta \frac{2Y_F}{Y_\infty} e^{(-d/L^*)} \left(1 + \left(1 - \frac{2Y_F}{Y_\infty}\right)\delta^2 + \left(1 - \frac{2Y_F}{Y_\infty}\right)^2 \delta^4 + \cdots\right) \right]$$

$$+ \left[(1 - \tau)\delta \frac{2Y_F}{Y_\infty} e^{(-d/L^*)} \left(1 + \left(1 - \frac{2Y_F}{Y_\infty}\right)\delta^2 + \left(1 - \frac{2Y_F}{Y_\infty}\right)^2 \delta^4 + \cdots\right) \right]^2$$

$$+ \Big[\qquad \Big]^3 + \cdots \Bigg\}$$

$$= \frac{Y_{io}\tau}{1 - \dfrac{(1 - \tau)\,\delta(2Y_F/Y_\infty)\, e^{(-d/L^*)}}{(1 - (1 - 2Y_F/Y_\infty)\,\delta^2)}} \qquad 3.8$$

Here the first term (unity) in the braces generates the probability of emission without a quantum-mechanical reflection at the interface. The additional yield terms (those in square brackets) are generated by tracing the possible future scenarios of the subset of hot-holes which approached the barrier with the requisite escape conditions, i.e. would be captured in the classical model, but were quantum-mechanically reflected away from the interface uniformly in all directions. The exponents of the bracketed terms equal the number of quantum-mechanical reflections experienced before capture.

At this point, the effects of those holes which suffer bulk phonon collisions are included. On average each bulk collision reduces the energy of the carrier by an amount $\hbar\omega$, higher energy carriers are scattered into lower energy states, so in effect the highest energy carriers are those that are lost. The yield is viewed as a sum of partial yields, where the nth partial yield represents the yield of the hot-holes which have suffered n phonon collisions. In this view the hot-holes are divided into distributions which are distinguished from one another by the number of phonon collisions experienced (phonon distributions). In terms of the escape cap, as the carriers lose energy, the spherical shell of excitation shrinks from the inside out.

Since a collision with a cold electron leaves a hot-hole unable to traverse the barrier, it is necessary to find the probability that a hole will collide with a phonon before a cold electron (γ), which is found to be

$$\gamma = \int_0^{\infty} e^{(-z/L_e)} \frac{1}{L_p'} e^{(-z/L_p')} dz = \frac{L_e}{L_e + L_p'} \qquad 3.9$$

Combining Equations 3.6, 3.7, 3.8, and 3.9 one obtains for the yield contribution of successive phonon distributions

$$Y = Y_0 + \left(1 - \frac{Y_0}{Y_\infty}\right)\gamma Y_1 + \left(1 - \frac{Y_0}{Y_\infty}\right)\left(1 - \frac{Y_1}{Y_\infty}\right)\gamma^2 Y_2 + \cdots \qquad 3.10$$

where the terms like $(1 - Y_n/Y_\infty)$ include the effects of holes which have been emitted on previous distributions, and the Y_n terms are the partial yields which are defined by a generalization of Equation 3.8 appropriate for the nth phonon distribution. This is done by redefining Equation 2.17 to reflect the energy loss of $n\hbar\omega$ for the nth phonon distribution, namely

$$Y_{Fn} = \frac{M(E_f - \Psi)^{\frac{3}{2}} + (E_f - (1+M)(h\nu - n\hbar\omega) + M\Psi)^{\frac{3}{2}} - (1+M)(E_f - h\nu + n\hbar\omega)^{\frac{3}{2}}}{2(E_f^{3/2} - (E_f - h\nu)^{3/2})(1 + M)} \qquad 3.11$$

and using Y_{Fn} rather than Y_F in Equation 3.8 to generate Y_n

The series of terms in Equation 3.10 is terminated when Y_{Fn} in Equation 3.11 becomes less than or equal to zero, that is when

$$n \geq \frac{h\nu - \Psi}{\hbar\omega} \qquad 3.12$$

One approximation still remains in these extended results. Due to depletion by preferential capture at the upper range of the energy distribution spectrum, each

successive phonon-scattered distribution is actually less uniform, i.e., more skewed toward lower energies, than its predecessor distribution. This effect is considered of second order and is neglected in Equation 3.10.

Characteristics of the Model

In this section the effects of the extensions to the modified Fowler equation are investigated through a series of Fowler plots. Fowler plots will be presented for ranges of thickness, mean free paths, and "phonon" energy loss relevant to Schottky infrared technology with the goal of presenting how the parameters impact the behavior of Fowler plots. The barrier height is taken as 0.2 eV., close to the value for PtSi on p-type Silicon. The parameters will be adjusted to fit the model to experimental data in chapter 5; however, at this point it is worth while to demonstrate that the extensions explain the anomalies in the experimental data from section 2.4.

Figure 17 shows a Fowler plot for a 20 Å diode with E_f=5 eV. $\hbar\omega$=0.01 eV., L_p'=70 Å, L_e=1000 Å, and τ=1. Superimposed on the Fowler plots is a line fit to the linear region of the curve. From Figure 17, it is evident that the barrier height as measured by extrapolating the linear region to the energy axis is about 0.06 eV. greater than the actual Schottky barrier height. If the thermal barrier height is interpreted as the Schottky barrier height, then the discrepancy between the optical and thermal barrier can

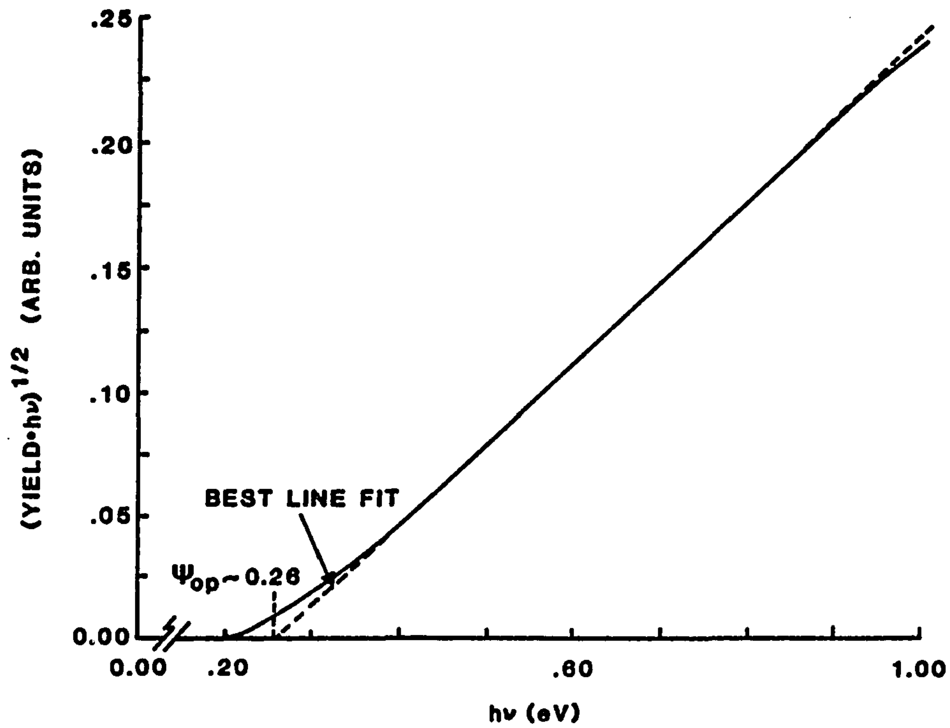

Figure 17. Fowler plot obtained using Equation 3.10 to determine the yield.

now be explained by using the extended model. Figure 17 also shows that the model can explain both the roll on and roll off in the Fowler plots for low and high photon energies. The roll on, and the difference between the barriers can be understood by examining the sum in equation 3.10. If the terms Y_n are approximated by a constant Y_o

$$Y_o = C_2 \frac{(h\nu - \Psi)^2}{h\nu} \qquad 3.13$$

where C_2 is approximately a constant if $2Y_F/Y_\infty$ is much less than unity. Then equation 3.10 can be written as

$$Y = C_1 Y_o \qquad 3.14$$

where

$$C_1 = \sum_{n=0}^{n_{max}} \left(1 - \frac{Y_o}{Y_\infty}\right)^n \gamma^n \qquad 3.15$$

with n_{max} given by

$$n_{max} = \frac{h\nu - \Psi}{\hbar\omega} \qquad 3.16$$

On a Fowler plot $\sqrt{Yh\nu}$ is plotted as a function of $h\nu$, where $\sqrt{Yh\nu}$ is given by

$$\sqrt{Yh\nu} = \sqrt{C_2}\,\sqrt{C_1}\,(h\nu - \Psi) \qquad 3.17$$

For the Fowler plot to be linear, the coefficient C_1 must be independent of photon energy. However as the photon energy is increased the number of terms in the expression for C_1 increases, leading to an increase in C_1. Since C_1 increases with increasing photon energy, the slope of the Fowler plot increases as the photon energy is increased, as shown in Figure 17 for photon energies near the barrier. As n_{max} becomes large, the successive terms in the sum approach zero, so that C_1 becomes a constant leading to a linear segment in Figure 17. In physical terms, the increase in C_1 is due to the fact that as the photon energy increases, the hot-holes can on average survive more phonon collisions and still escape.

The roll off at high photon energies is due to the yield approaching the theoretical limit value given by equation 3.6. Since the numerator in equation 3.6 is approximately linear in $(h\nu - \Psi)$, it will exhibit a square root dependency on a Fowler plot, giving the rolled off behavior.

Figure 18 shows the effect of L_p' on the Fowler plot. The optimal value of L_p' is found to depend on the photon energy, phonon energy loss and film thickness. For low excitation energy, few phonon collisions are necessary to thermalize the carrier, so longer L_p' values lead to higher yield. With increased excitation, the hole is less easily thermalized which increases the chances of it being

redirected into the escape direction before colliding with a cold electron. Hence more phonon collisions are desirable and a shorter L_p' leads to higher yields.

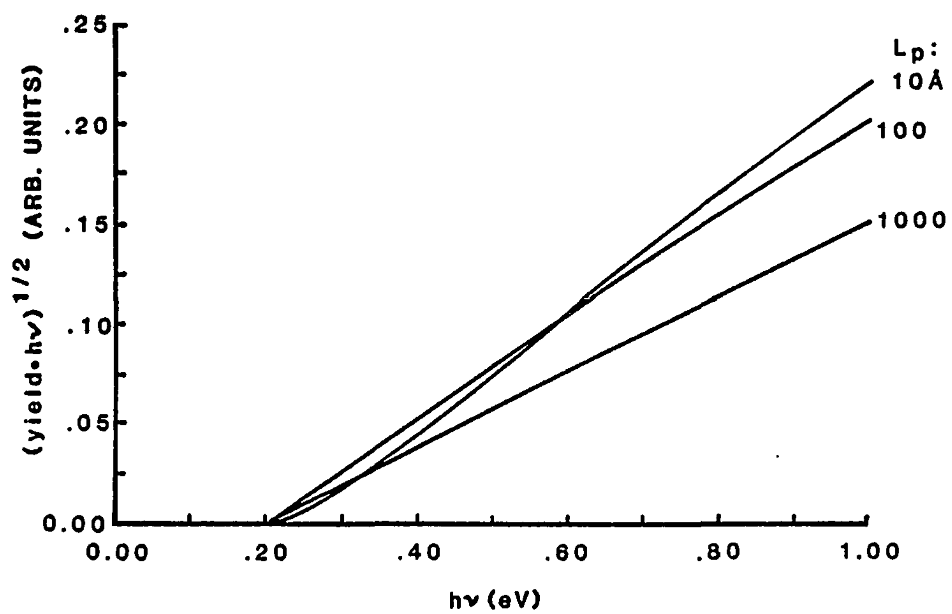

Figure 18. The effect of L_p' on the Fowler plots obtained using Equation 3.10.

Discussion of the Parameters in the Model

In this section the parameters which were defined in the previous sections are discussed. The range of values over which the parameters are expected to vary is estimated, and where appropriate, the sense in which the parameter is averaged is explicitly stated. The parameters addressed are the Fermi energy, the ratio of effective masses, the hot-hole/cold-electron mean free path, the hot-nole/"phonon" mean free path, the mean "phonon" energy, and the transmission coefficient.

The Fermi Energy

The Fermi energy is defined as the energy of the highest energy electron when the metal is in its ground state, as measured from the bottom of the conduction band. Unfortunately the Fermi energy in PtSi has never been measured; however in other materials its value is typically between 3 and 10 eV.[10].

The Ratio of the Effective Masses

The effective masses are included in the derivation of Equations 2.17 and 2.18 in an effort to estimate the volume of k space occupied by the excited states rather

than to determine the curvature of the energy band at any particular point. In this context, the definition of the effective mass for the metal is taken as

$$m_m = \frac{\hbar^2 k_f^2}{2E_f} \qquad 3.18$$

where $\hbar k_f$ is the magnitude of the momentum of an electron at the surface of the Fermi sphere. A similar definition can be made for the effective mass in the silicon.

Since the effective mass is usually defined in terms of the curvature of the energy band at the Fermi level, the value obtained from the literature may not be appropriate for this work. However at the present time this point is academic since the value of the effective mass for PtSi is not available in the literature.

It is reasonable to expect that the overall curvature of the energy bands does not vary drastically between the two materials, so the ratio between the two effective masses should be fairly close to unity.

The Hot-Hole/Cold-Electron Mean Free Path

The hot-hole/cold-electron mean free path in metals is not readily available in the literature. However it has been measured in gold[16,17] and should behave in a manner similar to the hot-electron/cold-electron mean free path. It can be shown[18,19,20,21,22] that the hot-electron/cold-

electron mean free path should vary as

$$\ell_e = \ell_o\left(\frac{E_f}{E}\right)^2 \qquad 3.19$$

where E is the hot-electron energy measured from the Fermi level. This dependence of mean free path on carrier energy has been observed for low electron energies

$$E \leq 1.5 \times 10^{-3} \text{ eV}. \qquad 3.20$$

however the dependence breaks down at higher carrier energies[23]. Figure 19 illustrates selected literature results on the ℓ_e versus E dependence in gold.

From Figure 19, it can be seen that the L_e defined in section 1 must be interpreted as an average of the mean free path over the energy range of interest. The average will be weighted toward the lower-energy hot-holes ($E \simeq \Psi$) since low-energy holes exist in the spherical shell of excited states for both a high-photon-energy and a low-photon-energy excitation, whereas high-energy holes only exist for the high-photon-energy excitation. The energy range of interest is from 0.2 to 1.0 eV above the Fermi level. Unfortunately there is very little data available over this energy region. The results of mean free path measurements on gold[24,25] and aluminum[26] indicate that the value of ℓ_e at 1.0 eV is at least 1000 Å. However in all

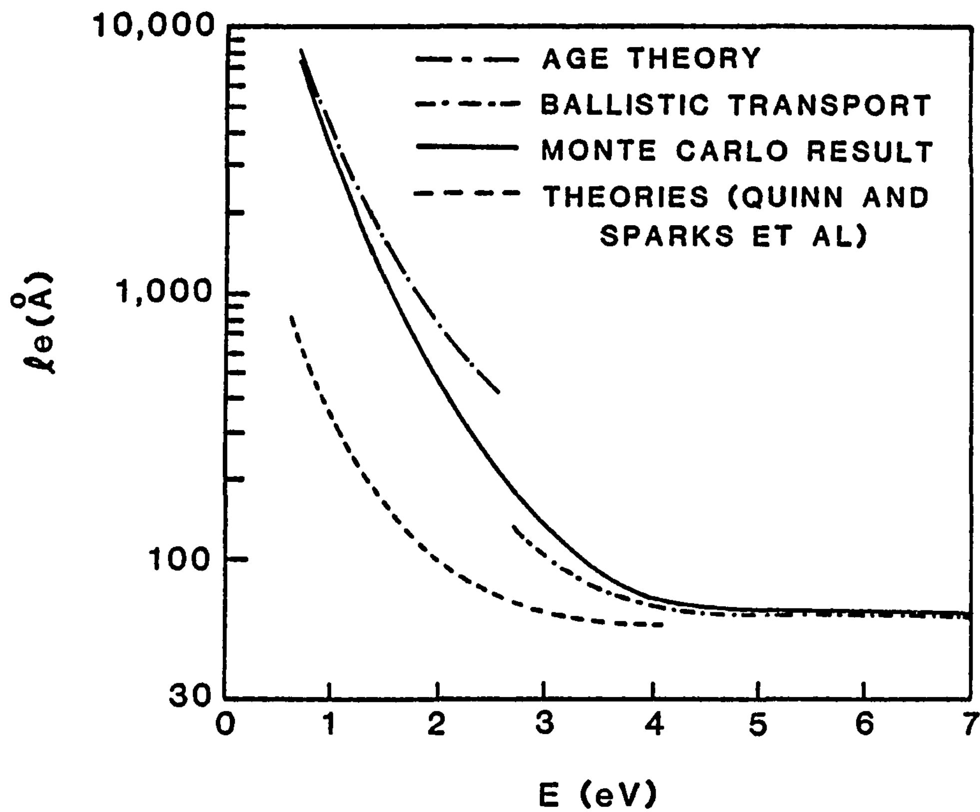

Figure 19. The hot-electron/cold-electron mean free path as a function of the energy of the hot-electron measured from the Fermi level.

Taken from reference 25.

cases the value of ℓ_e is a rapidly decreasing function of electron energy. Under the assumption that similar results can be expected for holes in platinum silicide and extrapolating the data in the literature to the energy range of interest, one estimates values of 5,000 to 50,000 Å for L_e to be appropriate.

The Hot-Hole/"Phonon" Mean Free Path

As was stated in section 3.1, this mechanism includes scattering events with phonons, impurities, dislocations, and other lattice imperfections. The collisions are all assumed to be semi-elastic; however, phonon scattering events require a greater exchange of energy than the other mechanisms. If (for example) three semi-elastic scattering mechanisms exist in the metal film, L_p' is given by

$$\frac{1}{L_p'} = \frac{1}{L_1} + \frac{1}{L_2} + \frac{1}{L_3} \qquad 3.21$$

where L_1, L_2, and L_3 are the mean free paths of the three scattering mechanisms. L_p' has been measured in gold, silver, copper, and palladium[25,27,28] to be between 100 - 500 Å.

The Mean "Phonon" Energy

The mean energy loss for a "phonon" collision is given by

$$\hbar\omega = \delta_1 \frac{L_p'}{L_1} + \delta_2 \frac{L_p'}{L_2} + \delta_3 \frac{L_p'}{L_3} \qquad 3.22$$

where δ_1, δ_2, and δ_3 are the energy losses associated with the three scatter types. The energy spectra of the phonons in PtSi has been measured using Raman spectroscopy[29,30]. Figure 20 shows that two lines are predominant at 0.01 and 0.017 eV.

The observed mean energy loss per semi-elastic scatter will obey Equation 3.22. If all the imperfection scatters are more elastic than the phonon scatters then the maximum value $\hbar\omega$ can achieve is expected to be on the order of 0.017 eV.

The Transmission Coefficient

The transmission coefficient (τ) is defined as the probability that a hot-hole in the escape cap traverses the barrier after reaching the interface. Ideally the value of the transmission coefficient would be unity; however it is reduced from unity by two effects. The first is that the wave nature of the electron interacts with the potential barrier, the impact of which was discussed in section 2.5 and shown in Figure 15. The second effect is that of the change in band structure across the barrier, which has the consequence that the holes which were in allowed states in the PtSi may not be in allowed states in the Si. As the

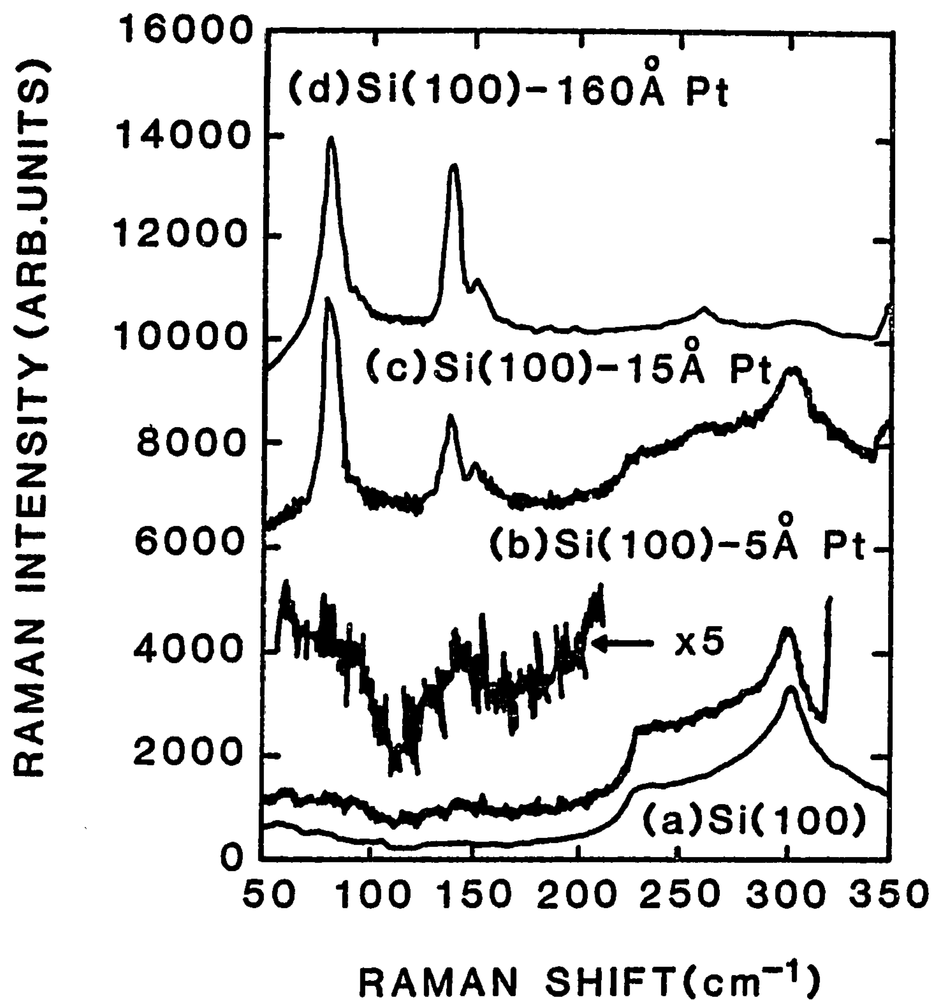

Figure 20. Raman spectra of Pt on Si after a 30 minute anneal at 500° C for three different thicknesses of Pt, and a bare silicon substrate.

Taken from reference 30.

holes in the forbidden states propagate in the silicon, the silicon lattice scatters the holes into different states. If the holes are scattered out of the escape cap prior to traversing the potential maximum, then they can no longer escape and are reflected back into the PtSi. If the holes traverse the barrier prior to being scattered, then emission has occurred. The scattering process will selectively scatter carriers out of the escape cap, since only holes which were initially in the cap can propagate far enough into the film to experience the lattice scattering.

The transmission coefficient has been treated in the literature[31]. For a reverse biased diode with typical dopant concentration, the transmission coefficient for electrons was found to be between 20 and 30%. Since the hot-hole mean free path in silicon is about a factor of two less than that of an electron[32], the transmission coefficient for holes is expected to be considerably less than that for electrons.

The scattering mechanism responsible for the redirection of the hot-hole momentum in the silicon has been determined to be scattering by optical phonons[31]. Since generation of optical phonons reduces the energy of the incident hot-hole, the loss of energy incurred by the phonon creation on the hot-hole should be included in Equation 3.8.

This modification was omitted, since its effects were determined to be of second order.

Chapter 4

OPTICAL ABSORPTION OF THE PHOTODIODES

Experimental Measurements

As was stated in chapter 1, the quantum efficiency of a photodiode depends on the product of the internal yield and the absorption (Equation 1.1). Chapter 3 addressed the internal yield and its effects on the quantum efficiency. This chapter will address the absorption.

The optical constants of PtSi have been determined over a fairly large spectral region for a relatively thick film (1400 Å of PtSi) by Pimbley and Katz[33]. Mahan and Marple[34] have extended Pimbley and Katz's work by using the optical constants to calculate the absorption as predicted by standard thin film optics and comparing the results with their own experimental measurements. Their data was taken at one wavelength over many different film thicknesses (18 - 480 Å of PtSi). The comparison is disappointing although not unexpected, since it is well documented that the optical properties of thin films are very sensitive to film microstructure which in turn is sensitive to slight changes in processing procedures[35,36]. For this reason the absorption

of the PtSi/Si photodiodes used in this work was measured rather than calculated from the optical constants.

In measuring the absorption of the PtSi film, it was assumed that the silicon substrate did not absorb any of the radiation. With this assumption the absorption in the PtSi film for backside illumination is computed from the expression (see Figure 21)

$$A' = 1 - R' - T \qquad 4.1$$

where R' and T are the backside reflection and transmission coefficients of the photodiode which can be measured directly. Losses due to scattering for the chemically polished silicon wafers are negligible[37]. Measurements of the reflection and transmission were performed over the 1.28 to 5.99 µm wavelength interval, which corresponds to the band edge of silicon and the Schottky barrier cutoff of the photodiode, respectively. From 1.28 to 2.5 µm, the measurements were performed on a Cary 14 spectrometer, while over the region from 2.5 to 5.99 µm, the measurements were performed on a Nicolett 7199A Fourier transform spectrometer.

The reflection measurements were made at near normal incidence for both front and backside illumination. On the Cary spectrometer, a Cary single pass reflection attachment was used; on the Nicolett, a Harrick variable angle

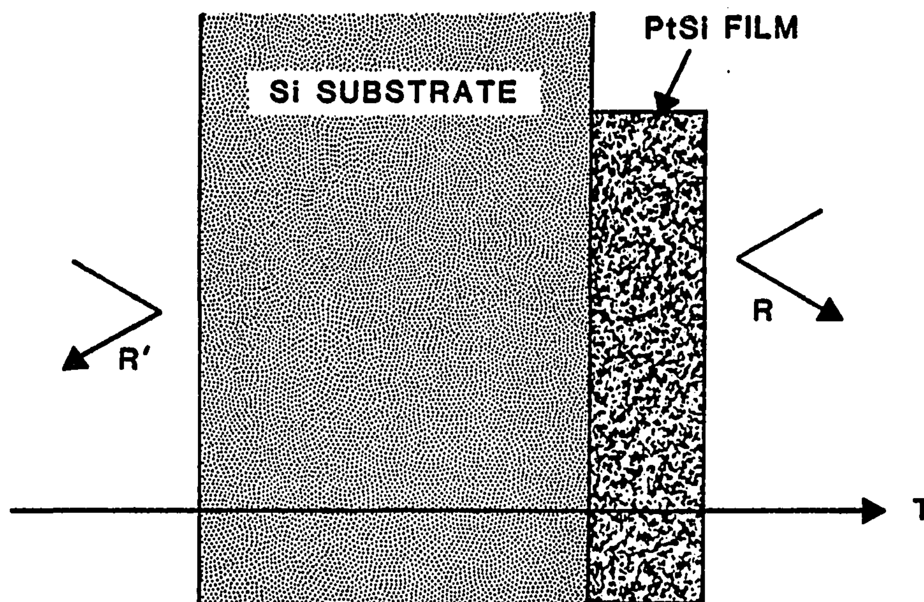

Figure 21. Diagram illustrating the definitions of R, R' and T.

single pass attachment was used. All of the measurements were reproducible to better than 2%.

Figures 22 - 27 illustrate the behavior of R, R', and T as a function of wavelength for a thin (20 Å) and a thick (400 Å) PtSi film. Figures 28 and 29 show how the absorption varies as a function of wavelength for the same two diodes. For the thin diode, the reflection and transmission characteristics are dominated by the effects of the silicon substrate which has a reflection of 46% and a transmission of 54% over the spectral region of interest (see Figures 22, 24 and 26). Since the refractive index of the silicon changes very little over this wavelength interval, only slight changes in the measured values as function of wavelength are observed. The diodes with the thick PtSi films show much more evidence of the effects of the platinum silicide (see Figures 23, 25 and 27). The reflection for both front and backside illumination increases substantially for increasing wavelength between 1.5 and 4 μm; while the transmission decreases over the same interval.

The characteristics of the absorption for the thin film (Figure 28) are spectrally flat, and hence will not effect the spectral characteristics of the diode response (Fowler plot). However since the absorption of the thick diode (Figure 29) is not uniform, the absorption

characteristics of this diode will impact the characteristics of the Fowler plot.

In chapter 5, the model for internal yield from chapter 3 is fit to the experimental data from this section and section 2.4 using Equation 1.1. However before fitting the data, it is worthwhile to estimate the errors in the absorption data. The next section will address these errors.

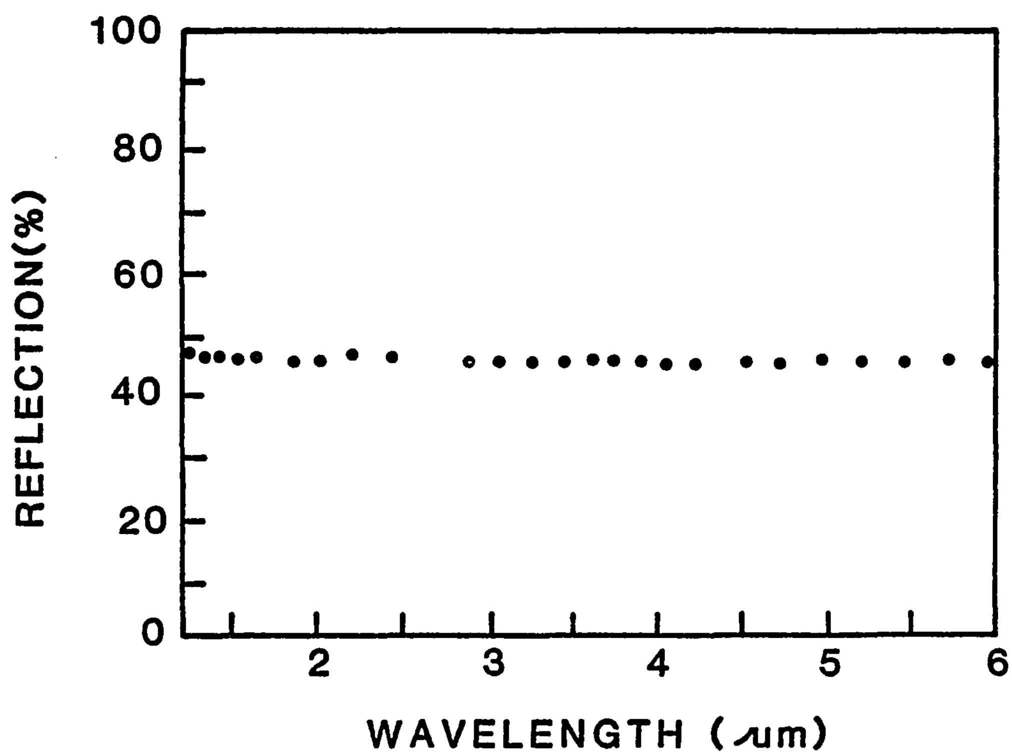

Figure 22. Frontside reflection as a function of wavelength for the diode with a 20 Å thick PtSi film.

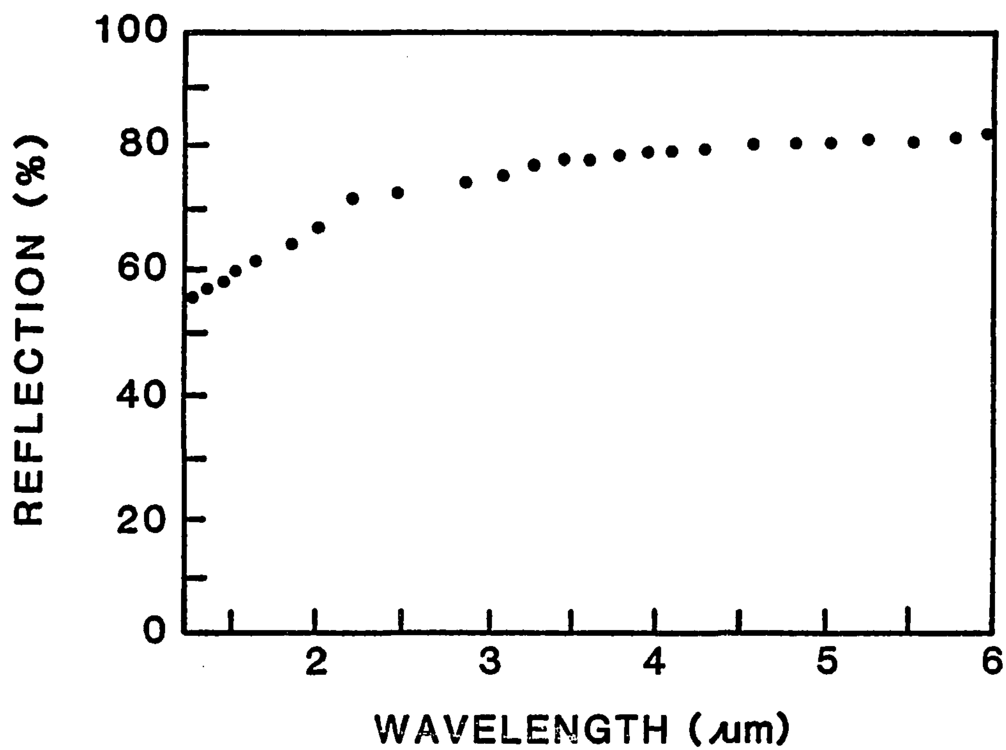

Figure 23. Frontside reflection as a function of wavelength for the diode with a 400 Å thick PtSi film.

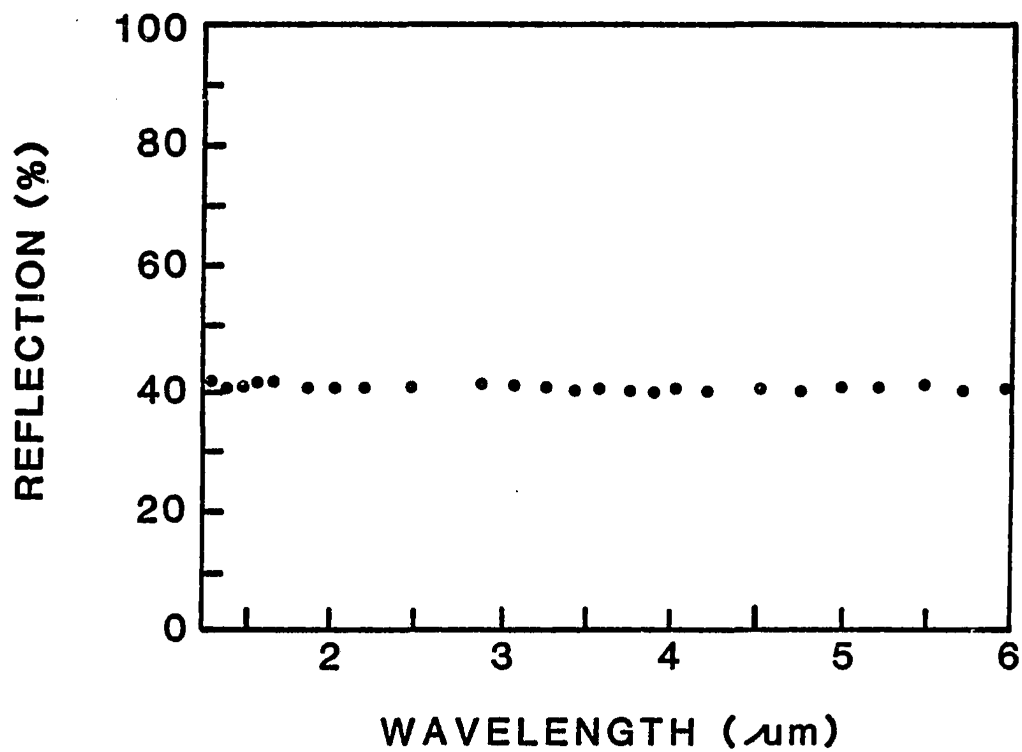

Figure 24. Backside reflection as a function of wavelength for the diode with a 20 Å thick PtSi film.

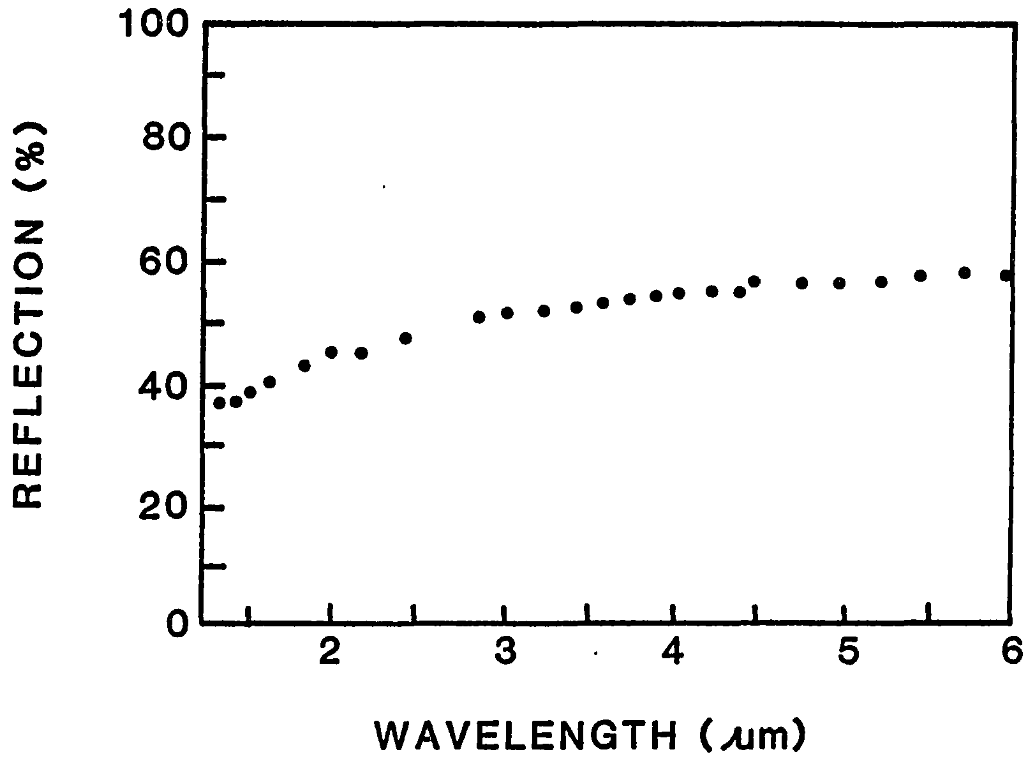

Figure 25. Backside reflection as a function of wavelength for the diode with a 400 Å thick PtSi film.

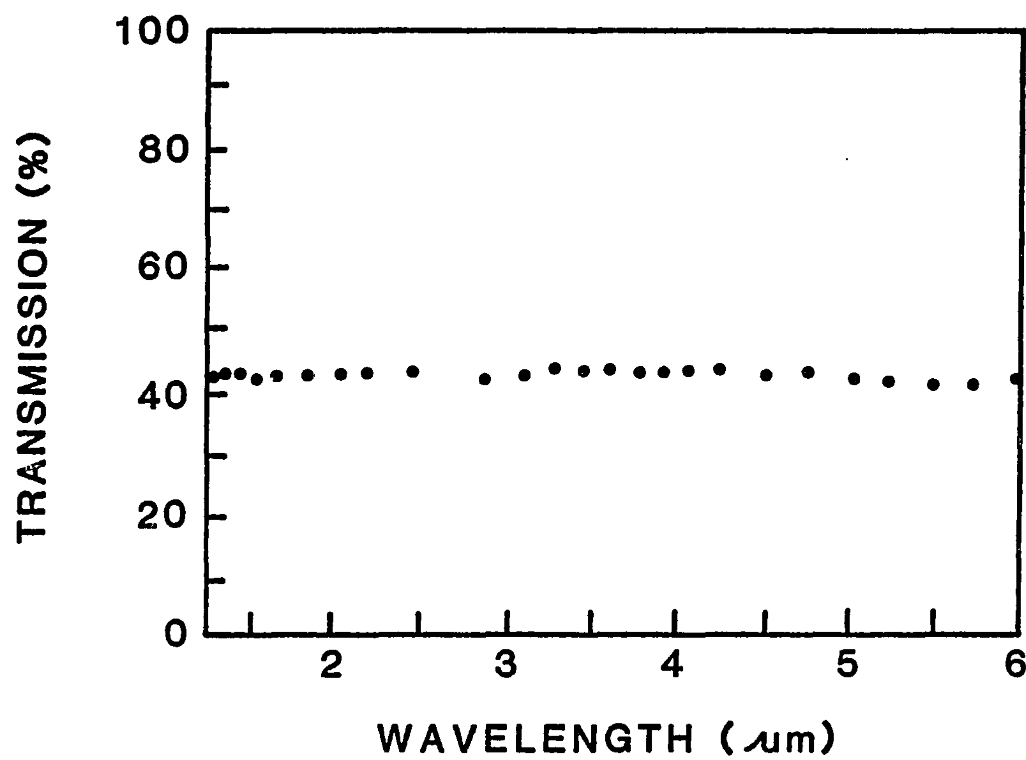

Figure 26. Transmission as a function of wavelength for the diode with a 20 Å thick PtSi film.

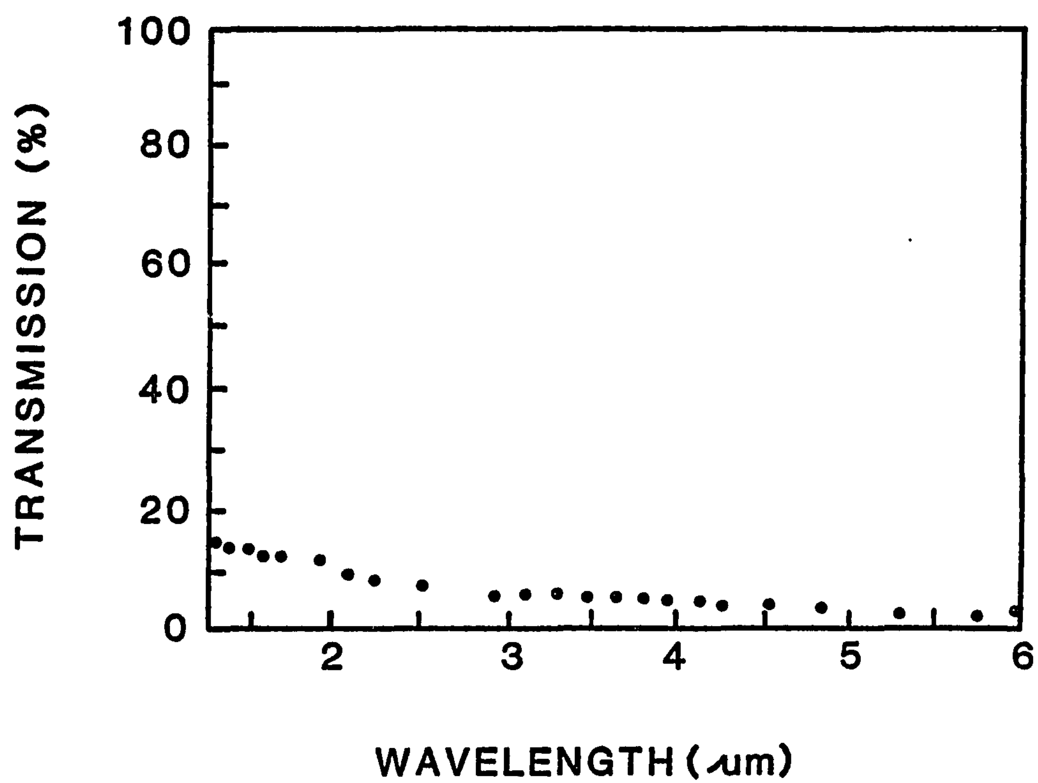

Figure 27. Transmission as a function of wavelength for the diode with a 400 Å thick PtSi film.

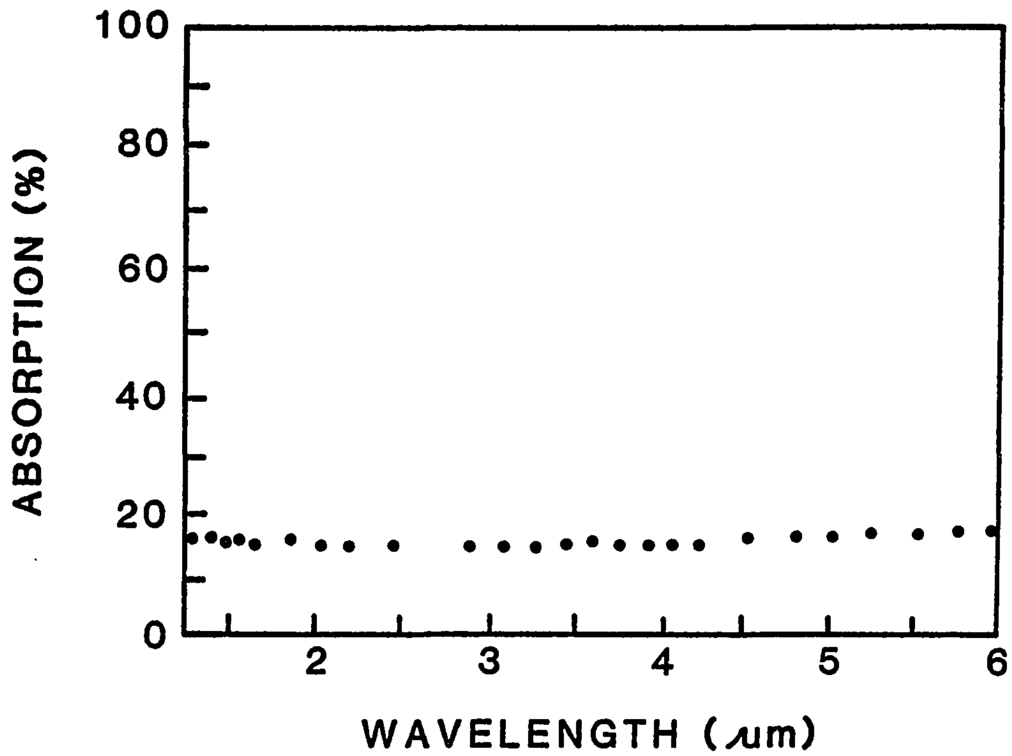

Figure 28. Absorption as a function of wavelength for the diode with a 20 Å thick PtSi film.

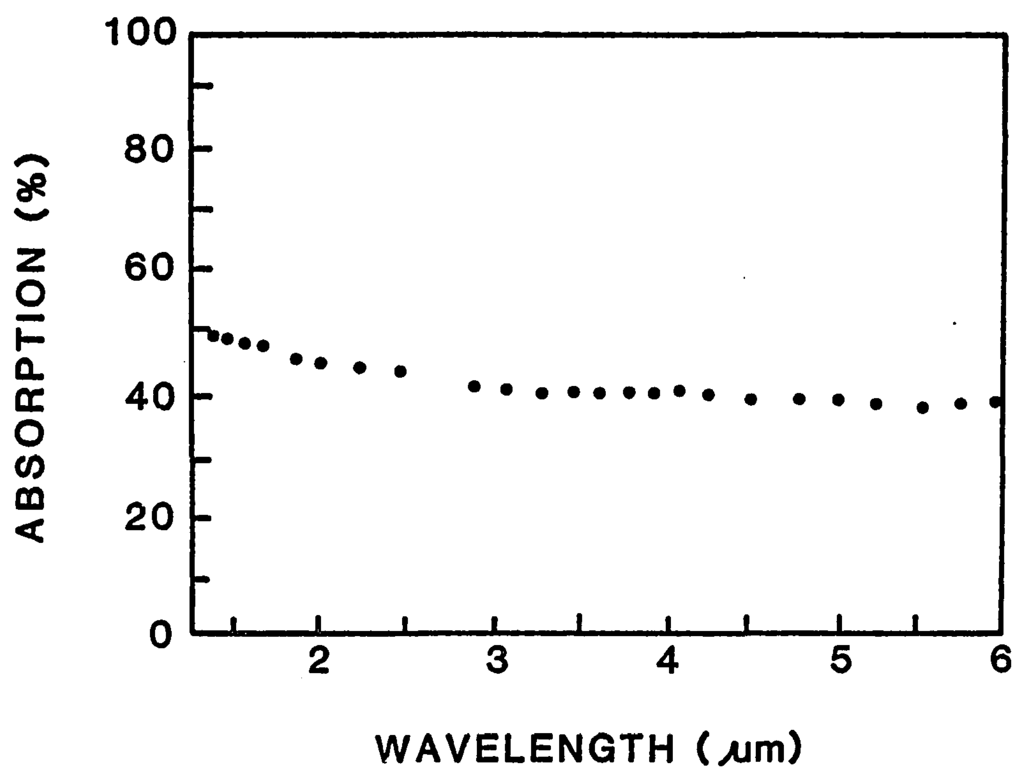

Figure 29. Absorption as a function of wavelength for the diode with a 400 Å thick PtSi film.

Error Analysis of the Absorption Data

The error analysis of the absorption data begins by recognizing that not only are errors introduced in the measurement of R, R' and T, but in the measurement of the film thickness as well. To quantify the magnitude of the errors, the measured values of R, R' and T were fit to the values predicted by thin film optics. The residual error between the predicted and measured values is then interpreted as an estimate of the error.

The equations needed to predict the optical characteristics of a Schottky barrier diode must treat two cases. The first treats the thin PtSi film, a case where the thickness is much less than the coherence length of the radiation, so that amplitudes of the electric fields of the multiple reflections in the film will add. The second case treats the silicon substrate with dimension much thicker than the coherence length of the radiation, and hence intensities rather than amplitudes of the multiple reflections are additive.

In the first (coherent) case the reflection and transmission coefficients are given by[36]

$$R_o = \left(\frac{n_iB - C}{n_iB + C}\right)\left(\frac{n_iB - C}{n_iB + C}\right)^* \quad 4.2$$

$$T_o = \frac{4n_in_{sub}}{(n_iB + C)(n_iB + C)^*} \quad 4.3$$

Where n_i is the index of the incident medium, n_{sub} is the index of the substrate and B and C are given by the matrix equation:

$$\begin{bmatrix} B \\ C \end{bmatrix} = \begin{bmatrix} \cos\xi & \frac{i\sin\xi}{n - ik} \\ i(n - ik)\sin\xi & \cos\xi \end{bmatrix} \begin{bmatrix} 1 \\ n_{sub} \end{bmatrix} \quad 4.4$$

where

$$\xi = \frac{2\pi(n - ik)d}{\lambda} \quad 4.5$$

Here (n - ik) is the complex index of refraction of the PtSi film, λ is the wavelength of the incident radiation, and d is the film thickness. For the case of frontside illumination, the reflection coefficient (R_o) is given by Equations 4.2, 4.4, and 4.5 where n_i and n_{sub} have been assigned the value of the index of air and the index of silicon respectively. For backside illumination the incident medium is silicon and the substrate is air, so in the calculation of the backside reflection coefficient (R_o')

the values of n_i and n_{sub} are exchanged. Figure 30 illustrates the difference between R_o and R_o'.

In the second (incoherent) case, the air/PtSi/Si system shown in Figure 30 can be treated as an effective interface with intensity transmission T_o and reflections R_o and R_o'. The intensity reflection coefficient for the silicon/air interface is given by

$$R_1 = \left[\frac{n_{Si} - 1}{n_{Si} + 1}\right]^2 \quad 4.6$$

where n_{Si} is the index of the silicon substrate. Since there no lossy medium at this interface, the reflection coefficient is independent of propagation direction.

The coefficients for the entire diode system are found to be:

For frontside illumination reflection

$$R = R_o + \frac{T_o^2 R_1}{(1 - R_1 R_o')} \quad 4.7$$

For backside illumination reflection

$$R' = R_1 + \frac{(1 - R_1)^2 R_o'}{(1 - R_1 R_o')} \quad 4.8$$

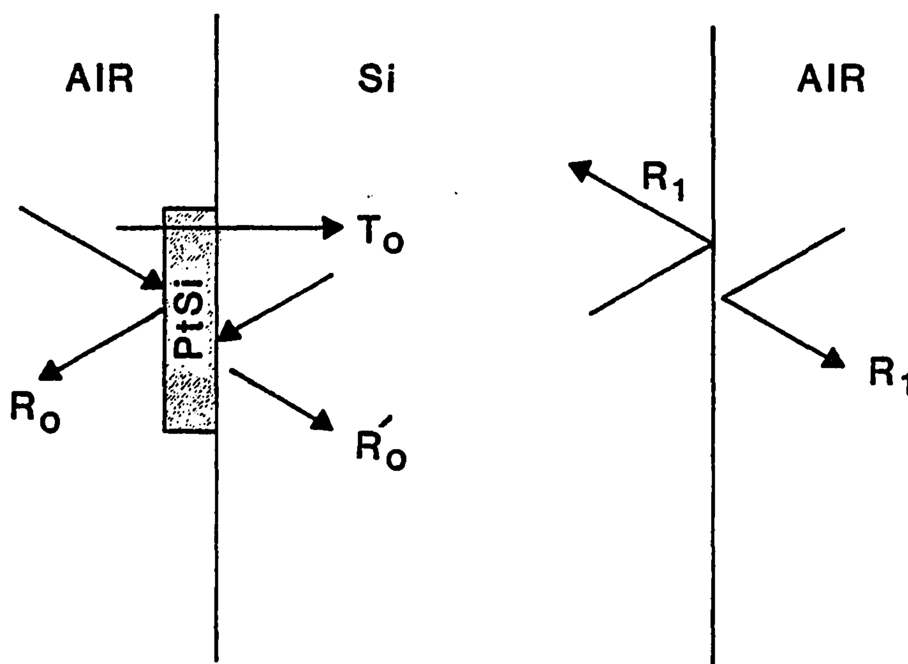

Figure 30. Diagram illustrating the definitions of R_o, T_o, R_o', and R_1.

For the transmission

$$T = \frac{T_0(1 - R_1)}{(1 - R_0' R_1)} \tag{4.9}$$

The value of the index of refraction for silicon is available in the literature[39]. The index of air is assumed to be unity, leaving the complex index of PtSi as an unknown. To find the complex index of PtSi, an optimization routine[40] was used to iteratively select values of n and k in Equations 4.2 - 4.9 with the intent of minimizing a merit function. The merit function is defined as

$$M_0(\lambda) = \sum_{\substack{\text{all} \\ \text{diodes}}} \left[(R_m - R)^2 + (R_m' - R')^2 + (T_m - T)^2 \right]^{1/2} \tag{4.10}$$

where R_m, R_m' and T_m are the measured values of the front and backside reflections and the transmission, and the sum is over all of the diodes. The optimization routine was constrained by the added requirement that the values of n and k be independent of thickness. This constraint was desirable since the ability to predict the absorption of a Schottky diode for an arbitrary thickness is a prerequisite to predicting its quantum efficiency. However, there is no guarantee that the constraint is physically meaningful.

Figures 31, 32, and 33 illustrate the frontside and backside reflections and the transmission as a function of thickness for 3.77 μm illumination. The solid line represents the expected values for the best fits of n and k. The curves show that the measured values of reflection and transmission do not deviate significantly for either the very thick or the very thin films. Since one value of n and k can adequately predict the measured reflections and transmission over a wide range of thicknesses, the constraint that n and k are independent of thickness is reasonable.

Close examination of Figures 31, 32, and 33 reveals that the 80 Å diode would fit the solid curves on the three plots much better if its thickness was actually on the order of 60 Å. Since three quantities were measured optically (R_m, R_m', and T_m), three quantities can be fit to the data. Having already fit n and k, one can allow the film thickness to vary, again with the intent of reducing the merit function. The best fit thickness values and those measured using the quartz oscillator are compared in Table 2. The mean percentage difference defined by

$$D = \frac{d_{osc} - d_{bestfit}}{d_{osc}} \qquad 4.11$$

was found to be D = 0.035 with a standard deviation

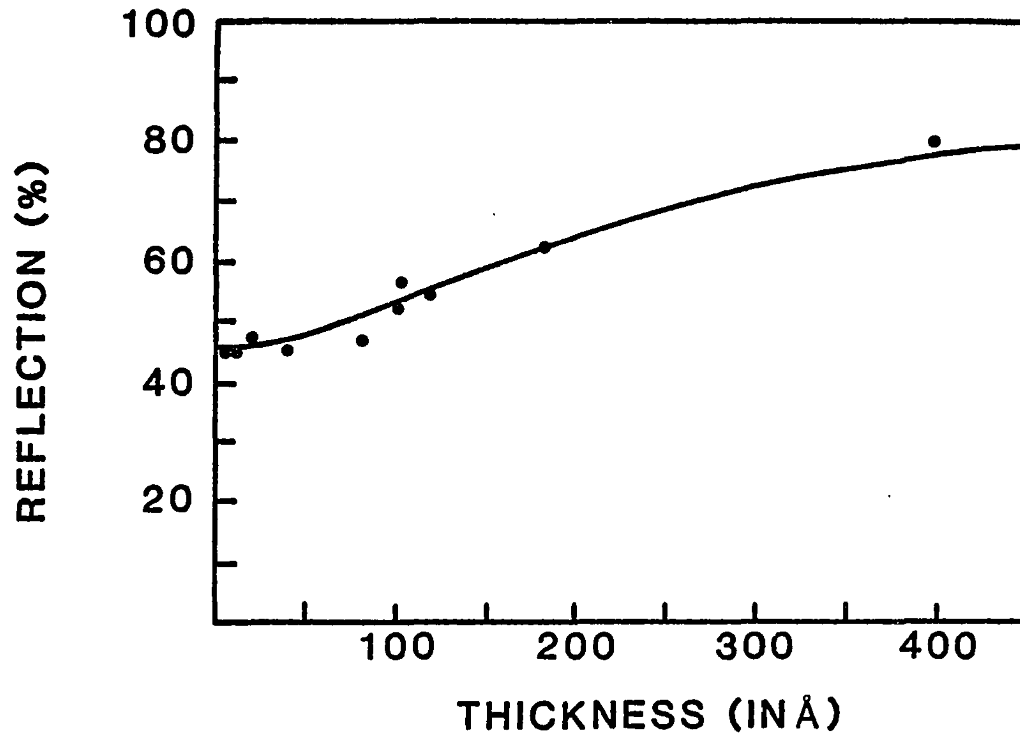

Figure 31. Frontside reflection as a function of PtSi film thickness for 3.77 μm illumination.

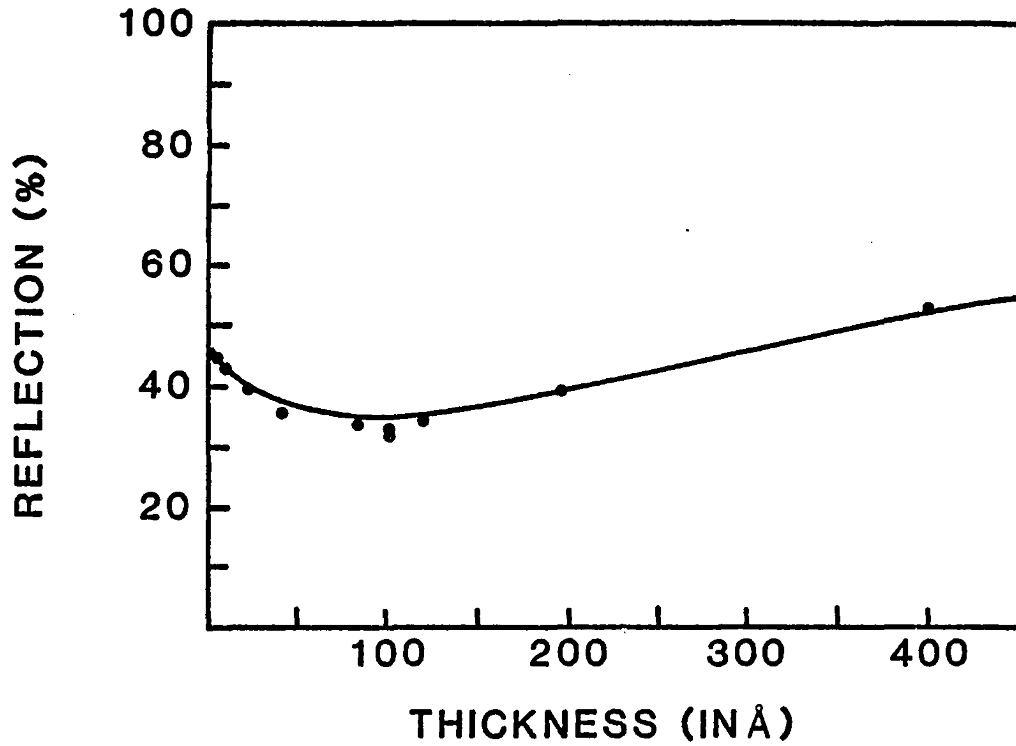

Figure 32. Similar to Figure 31 except the illumination is from the backside and Equation 4.8 is used.

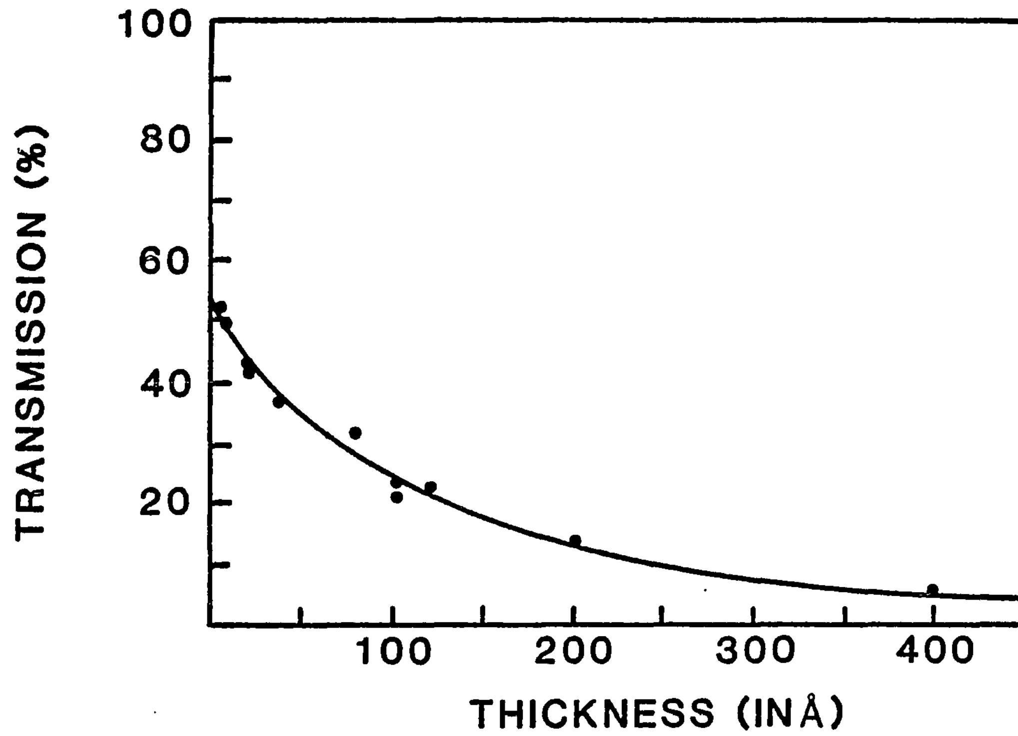

Figure 33. The transmission data fit using Equation 4.9.

Table 2. A comparison of the values of the thickness from the two different measurement techniques.

Diode Number	Thickness from Quartz Oscillator (Å)	Thickness from Best Fit to Optical Data (Å)
1	5	5.2
2	10	9.5
3	20	25.4
4	20	23.4
5	40	44.4
6	80	61.7
7	100	117.2
8	100	98.9
9	120	107.2
10	200	191.6
11	400	429.1

of σ_S = 0.14. The standard deviation is consistent with the expected errors in the quartz oscillator measurement system.

Figures 34, 35, and 36 illustrate the revised degree of fit between the measured data and the predicted values. A comparison with Figures 31, 32 and 33 demonstrates to what extent uncertainties in the thickness affect the fit.

The best-fit values of n and k along with the value of the merit function for the eleven diodes are shown in Table 3 for the best fit values for thickness. The error is accumulated over eleven diodes with three measurements per diode. From the accumulated error, the RMS error per measurement is estimated to be approximately 1.3% for reflection or transmission. For absorption the error will be the square root of two greater for an RMS error of 1.8%, which is consistent with the reproducibility which was reported in section 4.1.

Figures 37 and 38 show the absorption as a function of PtSi film thickness for the cases where the film thickness was determined by the quartz oscillator and by the best fit to the optical data, respectively. From the figures, it can be seen that at 3.77 μm the absorption goes through a maximum at about 230 Å of PtSi. The maximum in the absorption as a function of thickness is dependent on the wavelength of the incident radiation. For 1.28 μm radiation, a semi-infinite film has the greatest absorption; whereas for

6 μm radiation, the maximum occurs for films less than 200 Å thick.

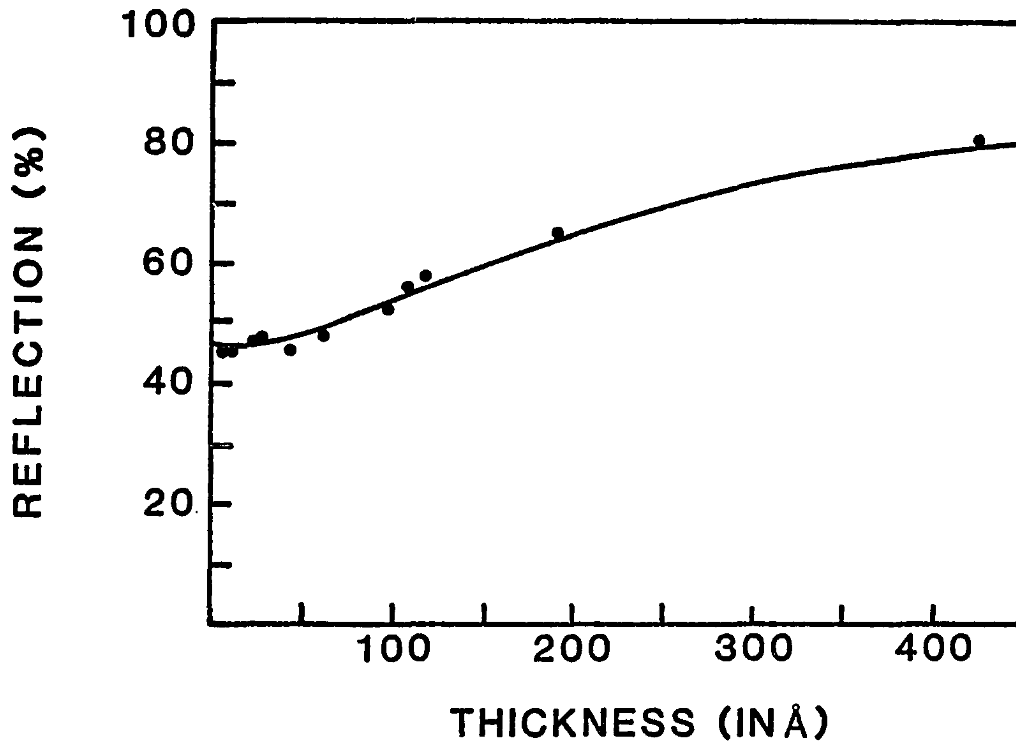

Figure 34. Similar to Figure 31 except the measured data has been adjusted by allowing the thickness of the diodes to vary until the error function (Equation 4.10) was minimized.

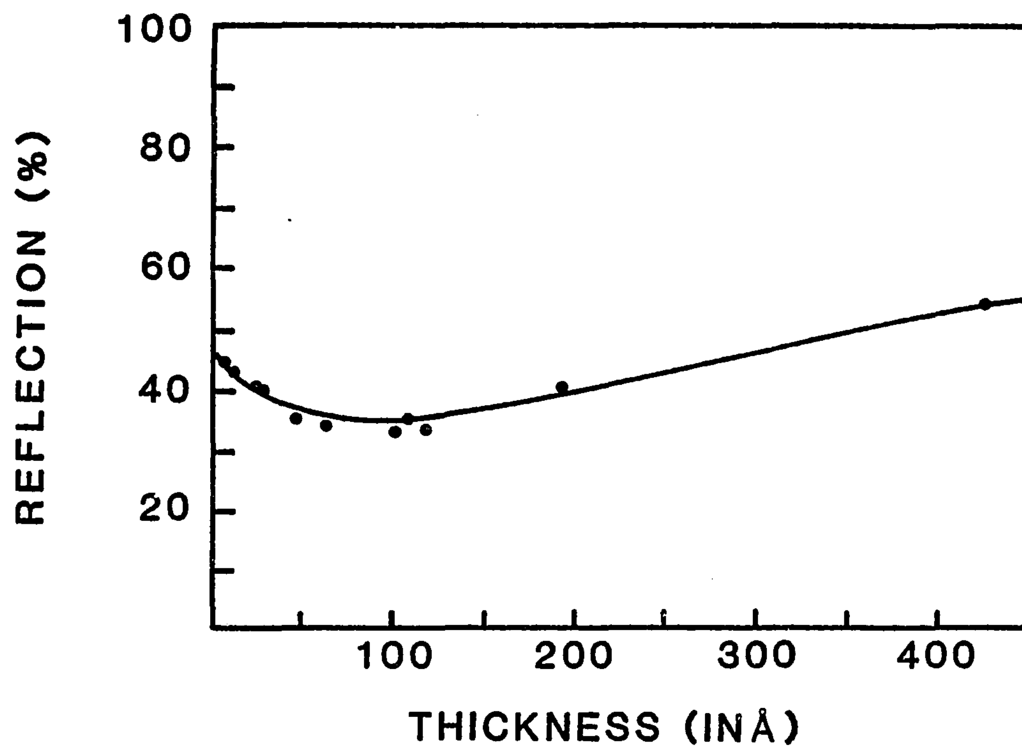

Figure 35. Similar to Figure 34 for backside reflection.

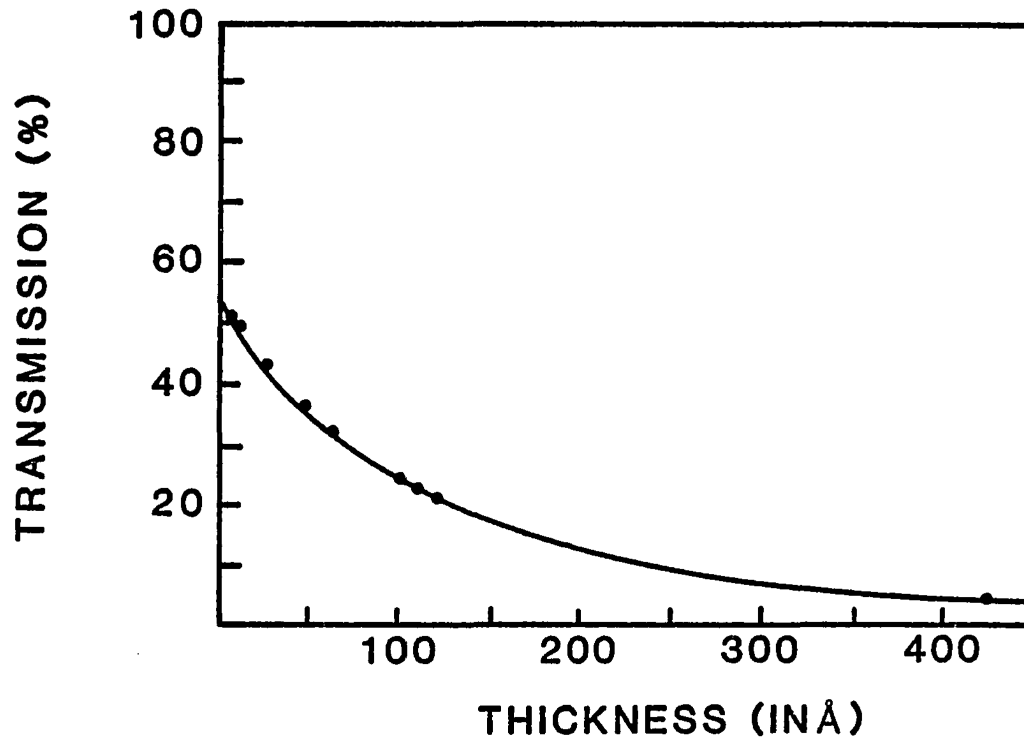

Figure 36. Similar to Figure 34 for transmission.

Table 3. The values of n and k which best fit the reflection and absorption data tabulated as a function of the incident photon wavelength.

Wavelength (μm)	n	k	$M_0(\lambda)$
1.28	4.51	2.44	0.097
1.37	4.88	2.42	0.091
1.46	3.21	3.85	0.099
1.55	3.09	4.25	0.094
1.65	3.06	4.65	0.091
1.85	3.05	5.47	0.084
2.03	3.15	6.12	0.074
2.20	3.25	6.67	0.084
2.45	3.52	7.44	0.062
2.88	3.80	8.98	0.050
3.07	3.91	9.42	0.043
3.26	4.08	9.86	0.046
3.44	4.25	10.30	0.050
3.60	4.39	10.67	0.053
3.77	4.54	11.05	0.054
3.92	4.70	11.38	0.057
4.07	4.90	11.70	0.057
4.25	5.11	12.08	0.059
4.52	5.43	12.66	0.064
4.77	5.68	13.13	0.068
5.01	5.90	13.62	0.071
5.25	6.16	14.09	0.077
5.50	6.40	14.54	0.081
5.74	6.58	14.96	0.084
5.99	6.72	15.43	0.089

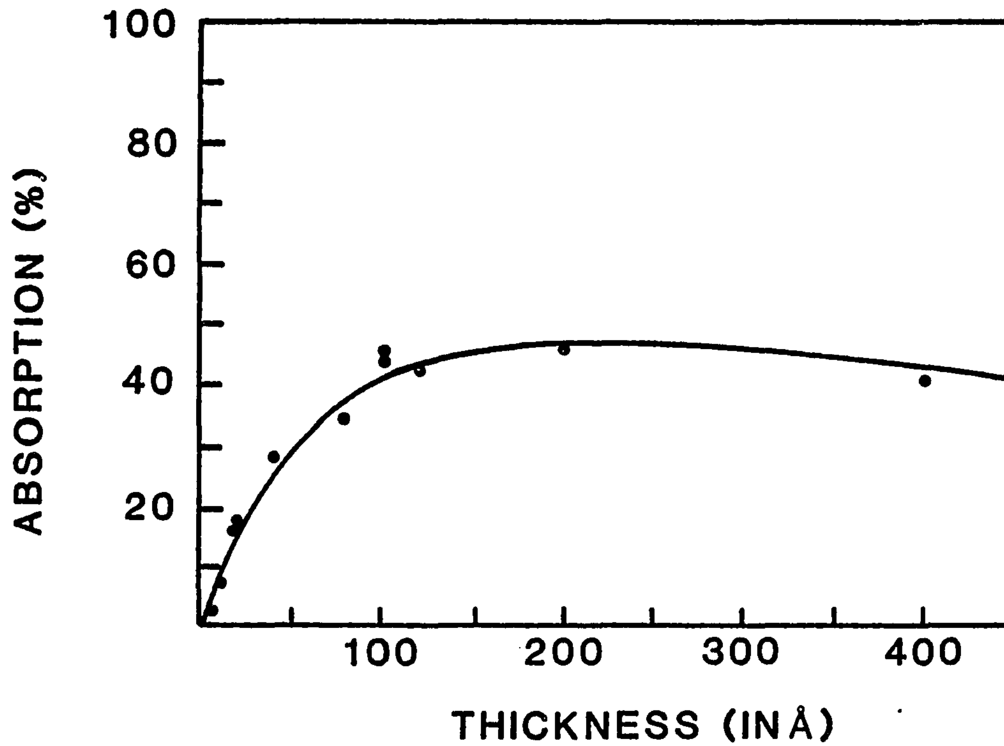

Figure 37. A comparison of the measured and calculated absorption as a function of PtSi film thickness.

Here the measured data is based on the film thickness as determined by the quartz oscillator.

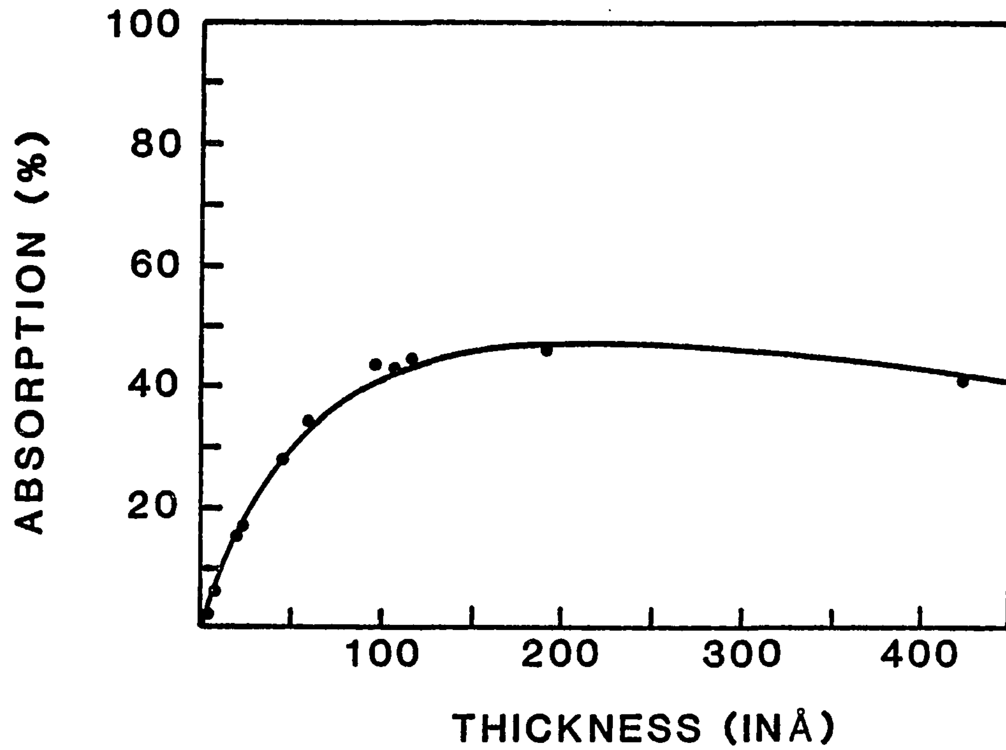

Figure 38. Similar to Figure 37 except the film thickness as determined by the optical best fits was used for the measured data.

Chapter 5

ANALYSIS OF THE MODEL

Initial Optimization with Two Free Parameters per Diode

In this chapter the data and theory of the previous three chapters are compared by finding the values of the parameters in the model which best predict the measured results. The parameters are found by using the simplex algorithm to minimize the mean squared error between the measured data and that predicted by the model. The optimization described in this section was not carried to completion, since it was found that the two free parameters were strongly correlated. The next section presents the completed optimization where the correlation is used to reduce the number of free parameters.

In order to relate the model for internal yield to the experimental measurements of quantum efficiency and absorption, the relation:

$$\frac{\eta_i(h\nu)}{A_i(h\nu)} = Y(d_i, \Psi_i, L'_{pi}, \hbar\omega_i, L_e, E_f, \tau, M, h\nu) \qquad 5.1$$

is used. Where the subscript i indicates the ith diode; $h\nu$ is the incident photon energy: d_i is the diode thickness as

determined in section 4.2; Ψ_i is the diode's barrier height measured using the activation energy technique; L'_{pi} and $\hbar\omega_i$ are the phonon collision mean free path and energy loss, respectively; L_e is the hot-hole/cold-electron mean free path ; E_f is the Fermi energy; τ is the quantum-mechanical transmission coefficient; and M is the ratio of the effective masses. Of these parameters, $h\nu$, d_i, and Ψ_i were determined prior to optimization; L'_{pi} and $\hbar\omega_i$ are assumed to be dependent on processing variations from diode to diode, while E_f, L_e and τ are assumed to be independent of processing; M is assumed to be unity (see section 3.3).

Since L'_p and $\hbar\omega$ are allowed to vary for each diode, and L_e, E_f and τ are constant over all the diodes, the overall optimization routine treats L'_p and $\hbar\omega$ separately from L_e, E_f and τ in that two nested optimization routines are used. In the inner loop L'_p and $\hbar\omega$ are varied to optimize the error function for each diode. The optimized error functions for each of the diodes are then summed and used as the error function for the selection of L_e, E_f and τ. The merit function for the optimization is defined by a least-square fit of the Fowler plots and is given by

$$M_T = \sum_i \sum_\lambda h\nu \left(\sqrt{\frac{\eta(\lambda,i)}{A(\lambda,i)}} - \sqrt{Y(\lambda,i)} \right)^2 \qquad 5.2$$

where the two sums are over the ten diodes and twenty five

different wavelengths. A flow chart for the optimization is shown in Figure 39.

When Equation 5.1 is applied to diode 1 (the thinnest diode), a problem is immediately encountered; the internal yield for the higher energy photons is greater than 100%. This result is not surprising since the measured absorption is 4% while its estimated error is 1.8%. The measured quantum efficiency on diode 1 is about 6% in this region. Since the estimated error is nearly as great as the measured absorption and the final result is not physically realizable, diode 1 was omitted in the analysis of the model.

Figure 40 shows $\hbar\omega$ as a function of L_p' for the solution L_e=7.78x10^4, E_f=11.9 and τ=0.0785. The line which best fits the data in Figure 40 has a slope of 1.01 which indicates that $\hbar\omega$ is nearly linearly related to L_p'. The relationship between L_p' and $\hbar\omega$ can be understood in terms of a physical model if the phonon scattering mechanism is broken into two parts. The two constituent phonon scattering mechanisms are characterized by a fairly lossy and an elastic scattering mechanism with mean free paths and energy losses given by L_p, δ_p, L_i, and δ_i. It is assumed that the lossy mechanism is due to true phonon scatters and is an inate characteristic of the metal film unaffected by the processing. The elastic mechanism is dominated by the

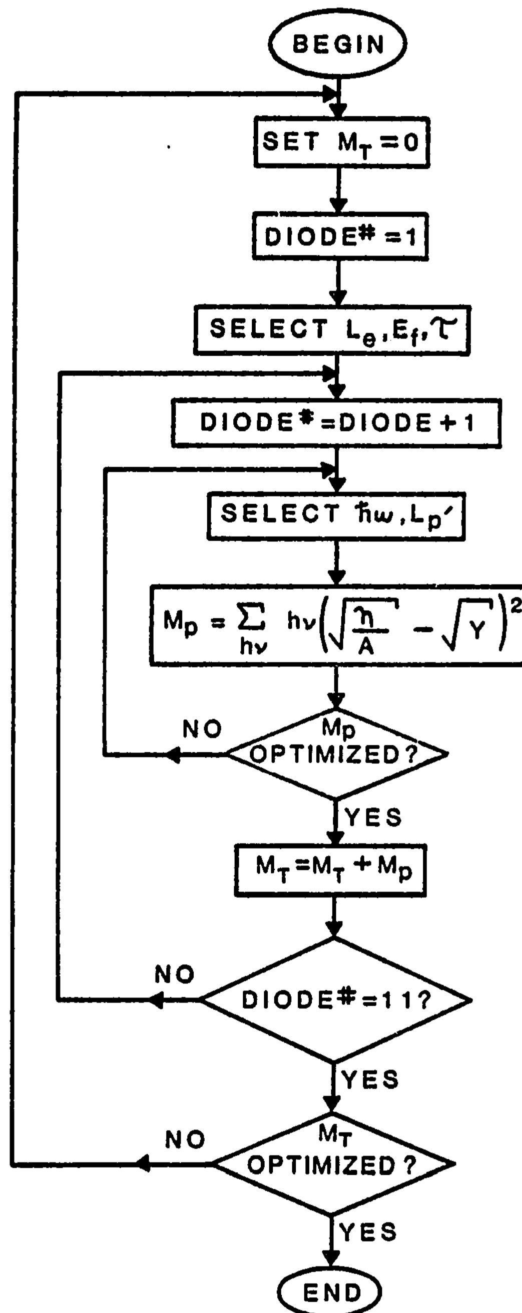

Figure 39. Flow chart of the routine used to find the values of E_f, L_e, τ, L'_{pi}, and $\hbar\omega_i$.

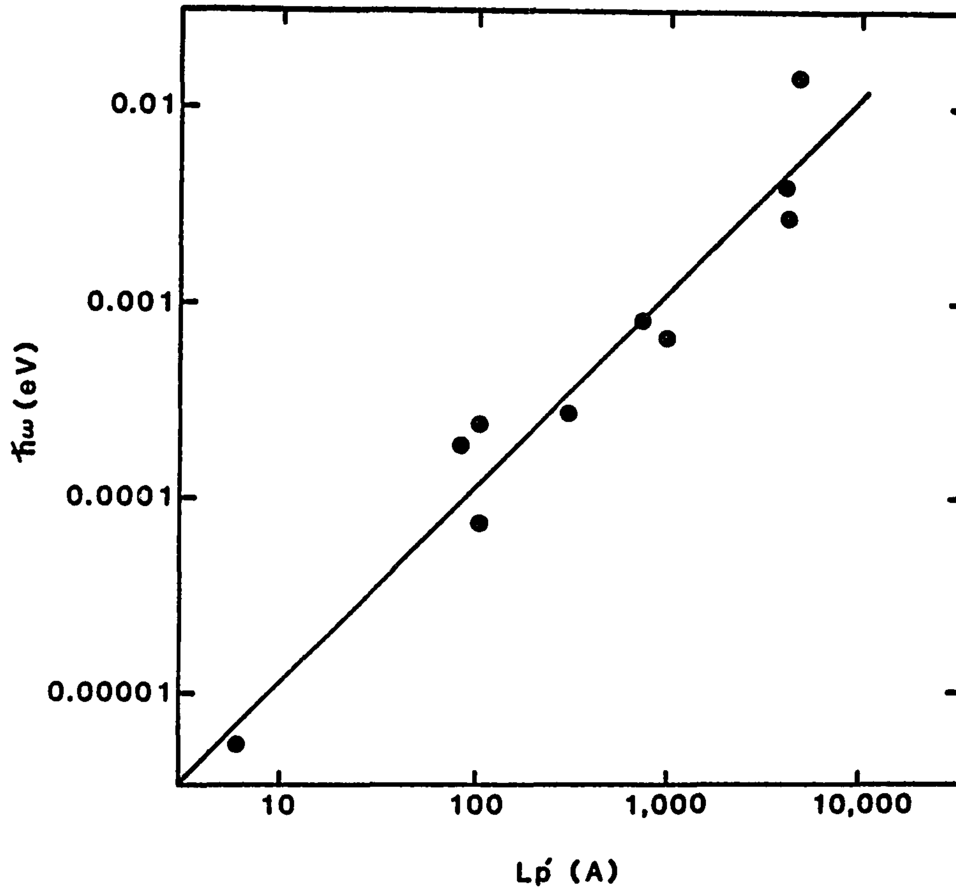

Figure 40. A log-log plot of $\hbar\omega$ as a function of L_p' for the ten diodes used in the optimization routine.

effects of imperfections in the metal film. The energy loss per elastic scatter (δ_i) is assumed to be zero, while the mean free path between elastic scatters is assumed to depend on processing. Hence L_p, and δ_p are expected to be constant over the diodes, while L_i may well vary from diode to diode.

L'_p and $\hbar\omega$ can be determined from L_p, δ_p and L_i using the techniques in section 3.3. L'_p is given by

$$\frac{1}{L'_p} = \frac{1}{L_p} + \frac{1}{L_i} \qquad 5.3$$

while $\hbar\omega$ is found to be

$$\hbar\omega = \frac{\delta_p}{L_p} L'_p \qquad 5.4$$

Since both δ_p and L_p are assumed to be constant for all the PtSi films $\hbar\omega$ is linearly related to L'_p. From Figure 40 and using Equation 5.4 the value of δ_p/L_p is found to be 1.1×10^{-6} eV/Å.

Optimization with One Free Parameter per Diode

In the previous section it was found that $\hbar\omega$ and L_p' are nearly linearly related, and that the relationship could be physically modeled by a combination of two distinct scattering mechanisms, as described mathematically by Equations 5.3, and 5.4. In this section, Equations 5.3 and 5.4 are incorporated into the optimization routine to determine how well the two scattering mechanism model can match the measured data.

The incorporation of the dual-scatter model into the optimization routine is accomplished by selecting E_f, L_e, τ, L_p, and δ_p in the outer loop, and only L_i in the inner loop. Equations 5.3, and 5.4 are used to calculate $\hbar\omega$ and L_p' from these parameters; while the equations used for calculation of the merit function are unchanged. There are two advantages of this approach compared to that used in the previous section. The first is that the imperfection mean free path (L_i) is the only free parameter allowed to vary from diode to diode. The second is that much of the ambiguity involved in the definition of $\hbar\omega$ and L_p' is removed since L_p and δ_p are associated with true phonon collisions and L_i is the

mean free path of only the imperfection scattering mechanisms.

The fits obtained using this approach are shown in Figures 41(a - j), while the parameter values used for the fits are listed in Tables 4 and 5. Also listed in the tables are the range over which the values of the parameters can vary and impact the merit function by less than 10%. In the figures, the measured internal quantum yield is shown as a sequence of dots; while the predictions of the model based on the parameters obtained from the optimization routine are shown as a solid line. The fits are presented as absorption corrected Fowler plots.

From the figures, it can be seen that the agreement between the model and the experiment is fairly good. Diodes with high internal yields exhibit the roll off at high photon energies, while all diodes exhibit the roll on for low photon energies. In all cases, the linear region of the Fowler plot extrapolates to a barrier height which is greater than the thermal barrier.

The fact that only the devices with high internal yields exhibit the roll off at high photon energies indicates that the energy dependence of L_e is not responsible for the roll off. If L_e were responsible for the roll off, the same characteristics would be observed for each diode.

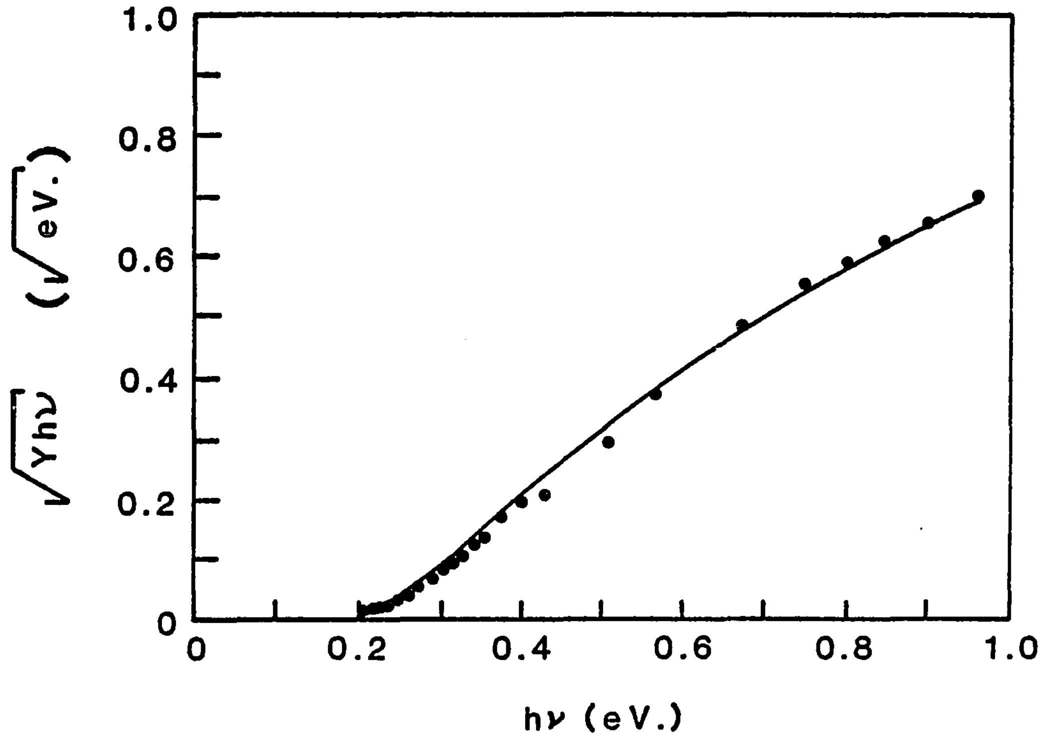

Figure 41(a). A Fowler plot for the internal yield of diode 2 showing both the measured data and the predictions of Equation 3.10.

The value of the partial merit function for this diode was 0.0631.

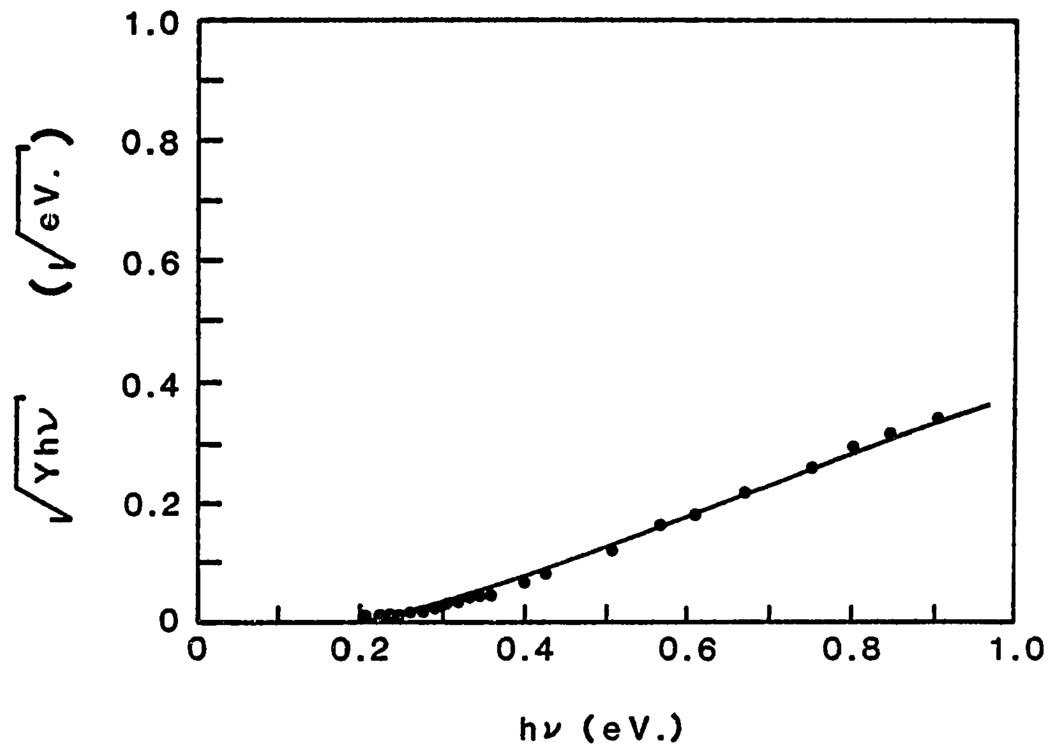

Figure 41(b). Similar to Figure 41(a) for diode 3.

The value of the partial merit function for this diode was 0.0368.

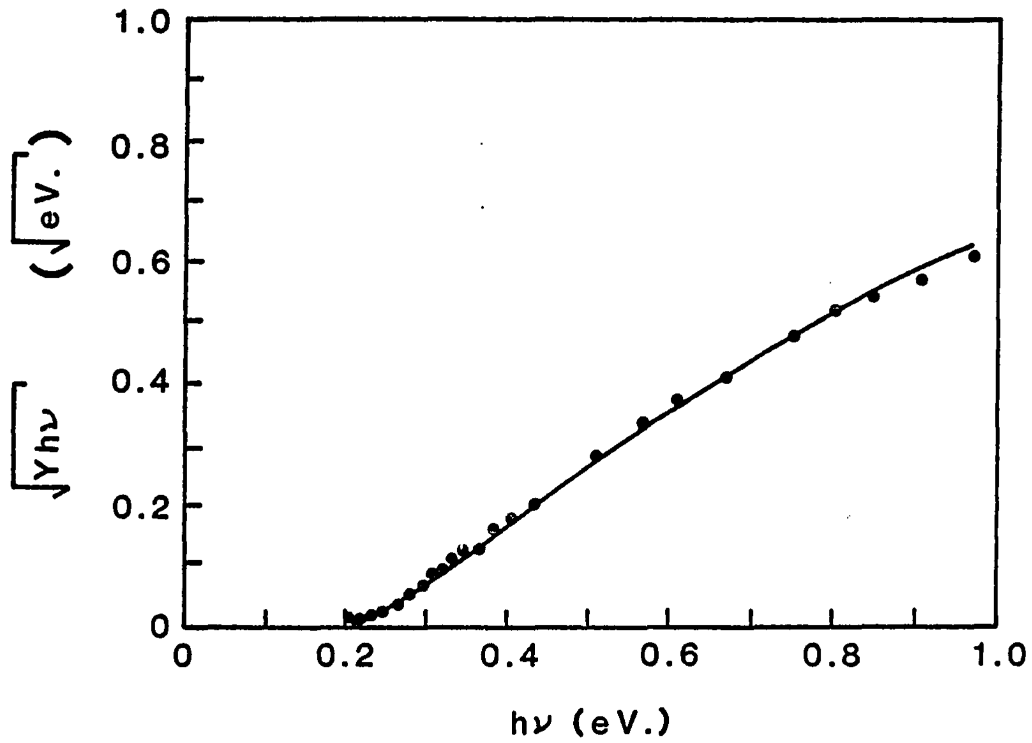

Figure 41(c). Similar to Figure 41(a) for diode 4.

The value of the partial merit function for this diode was 0.0462.

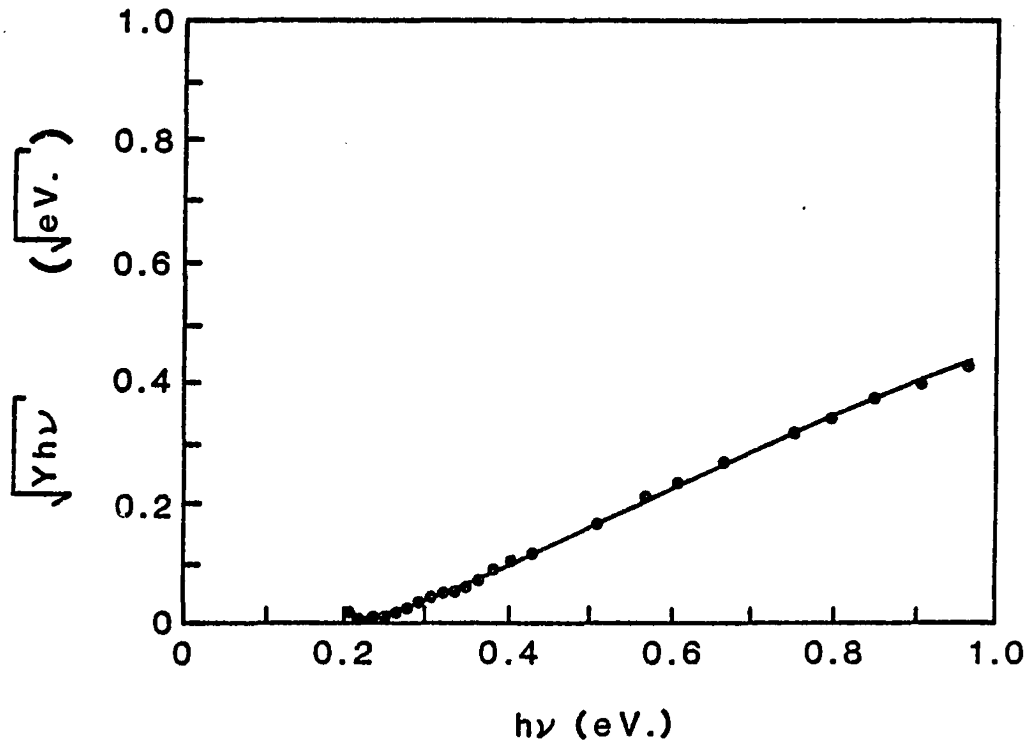

Figure 41(d). Similar to Figure 41(a) for diode 5.

The value of the partial merit function for this diode was 0.0245.

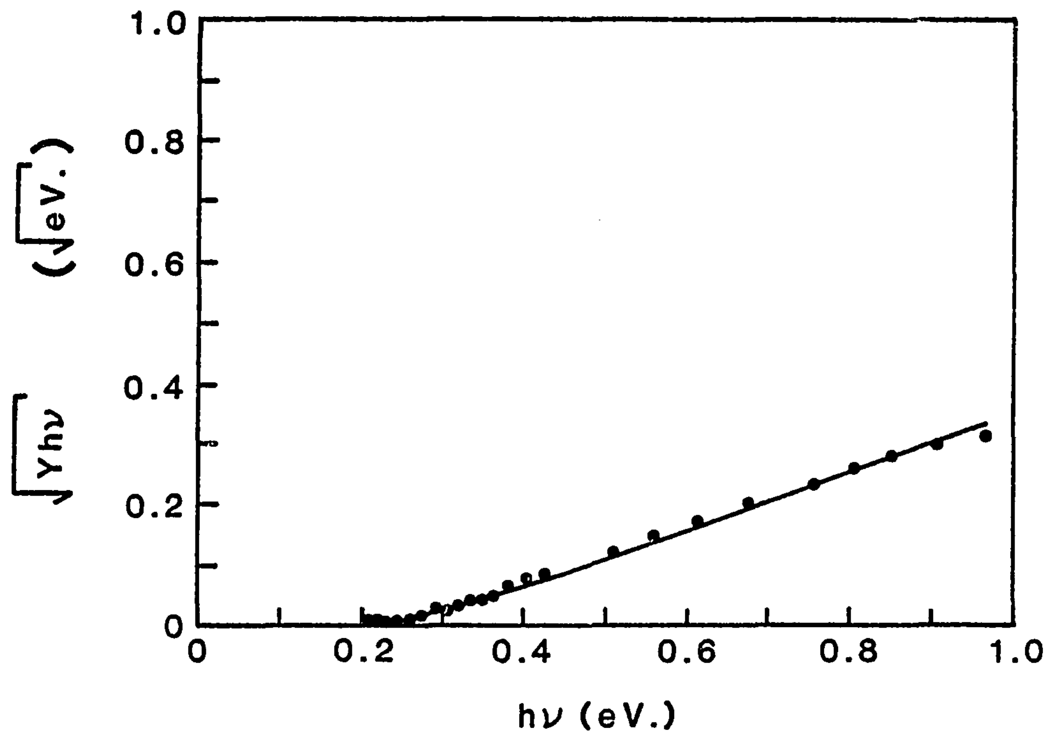

Figure 41(e). Similar to Figure 41(a) for diode 6.

The value of the partial merit function for this diode was 0.0328.

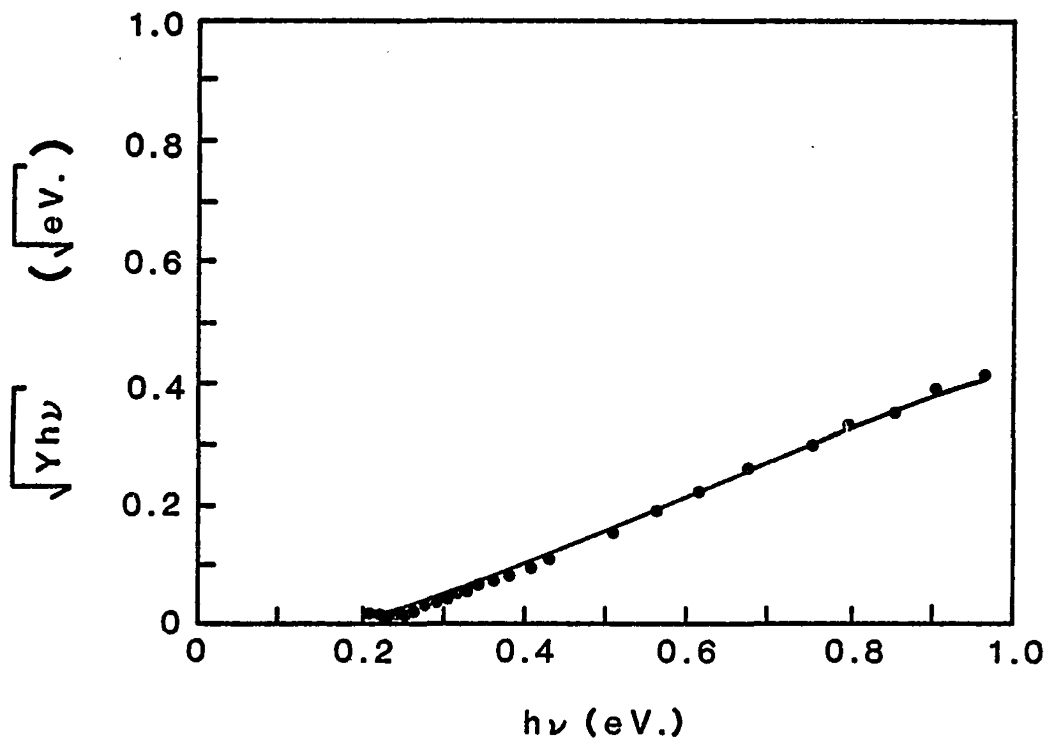

Figure 41(f). Similar to Figure 41(a) for diode 7.

The value of the partial merit function for this diode was 0.0307.

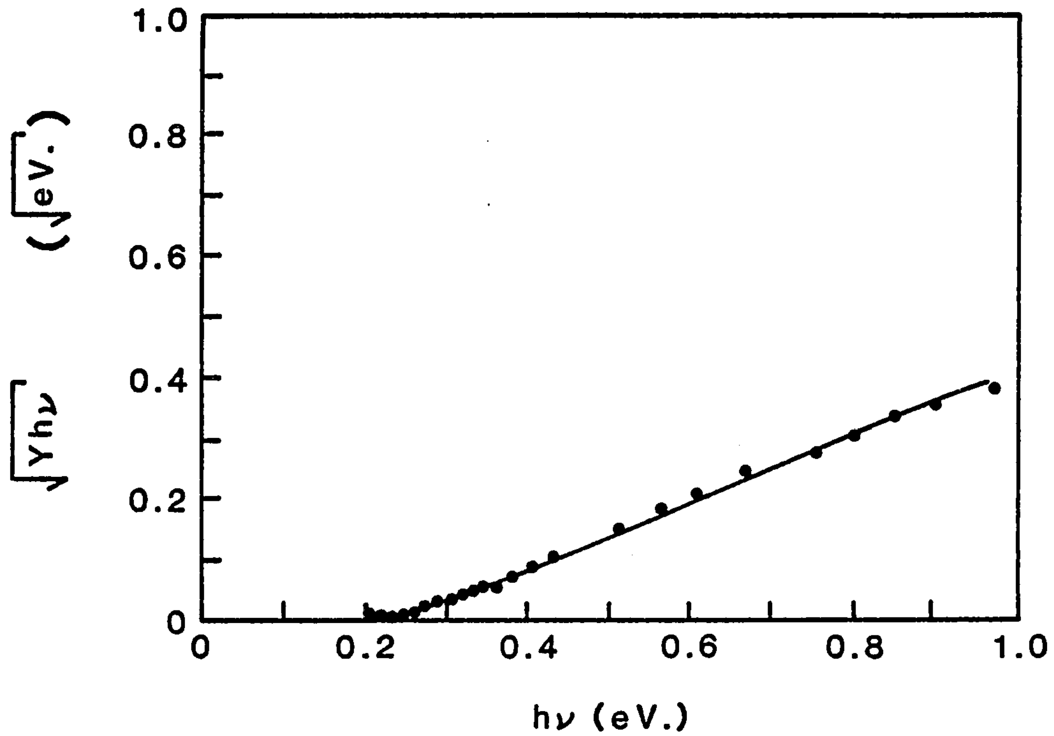

Figure 41(g). Similar to Figure 41(a) for diode 8.

The value of the partial merit function for this diode was 0.0290.

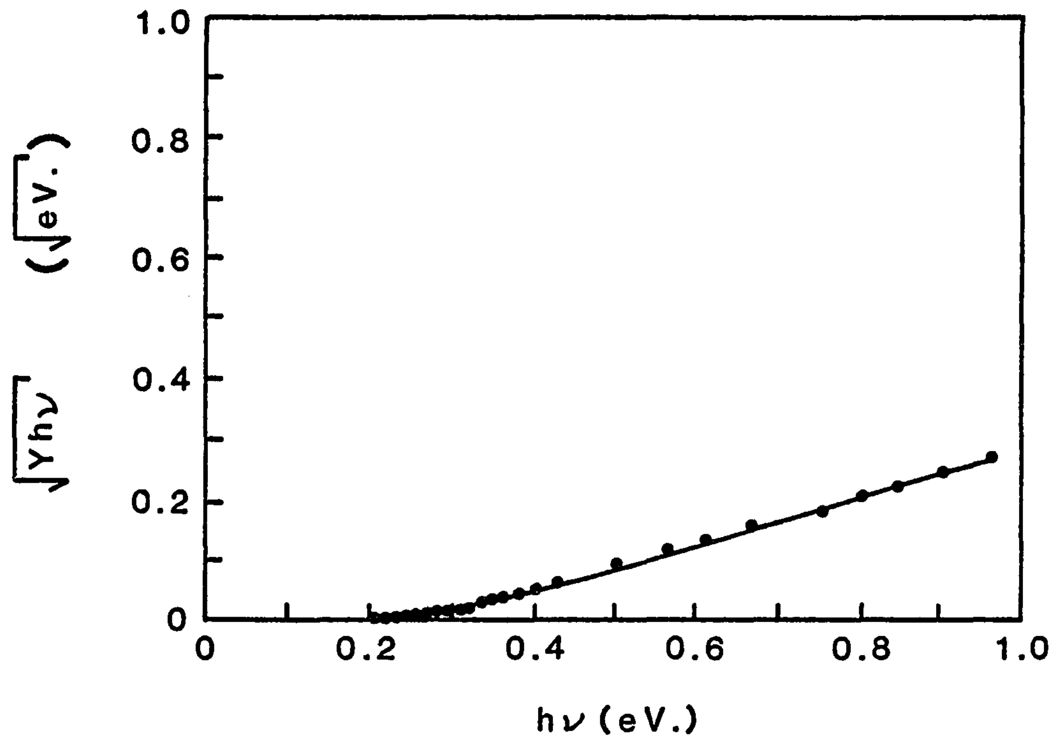

Figure 41(h). Similar to Figure 41(a) for diode 9.

The value of the partial merit function for this diode was 0.0143.

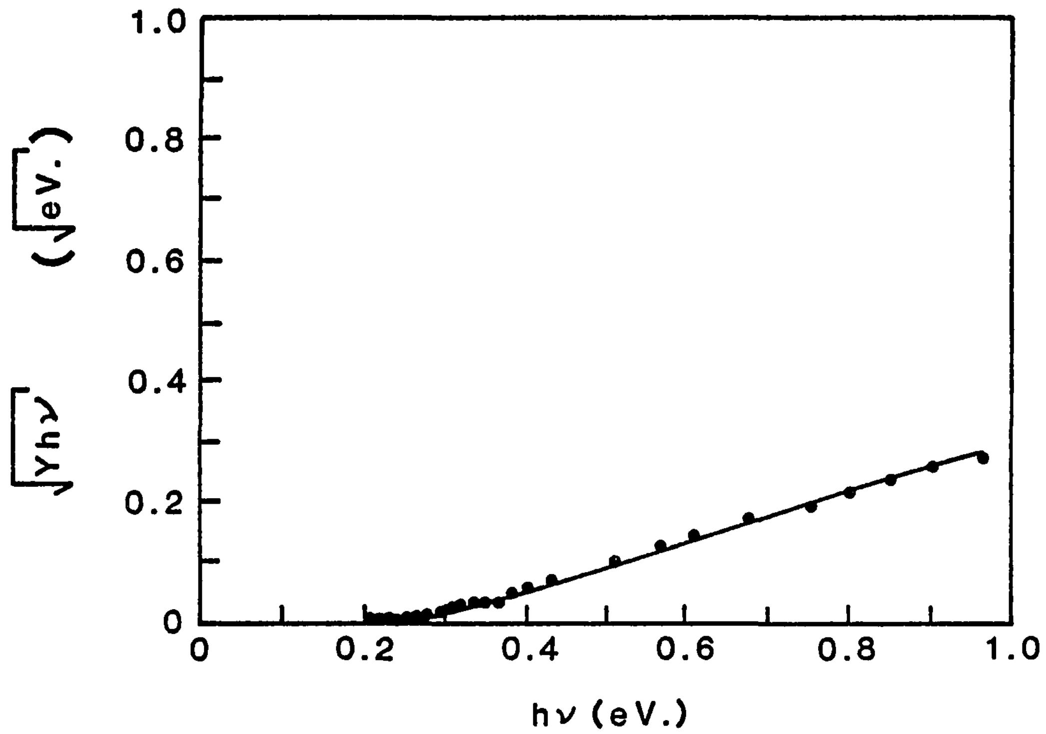

Figure 41(i). Similar to Figure 41(a) for diode 10.

The value of the partial merit function for this diode was 0.0198.

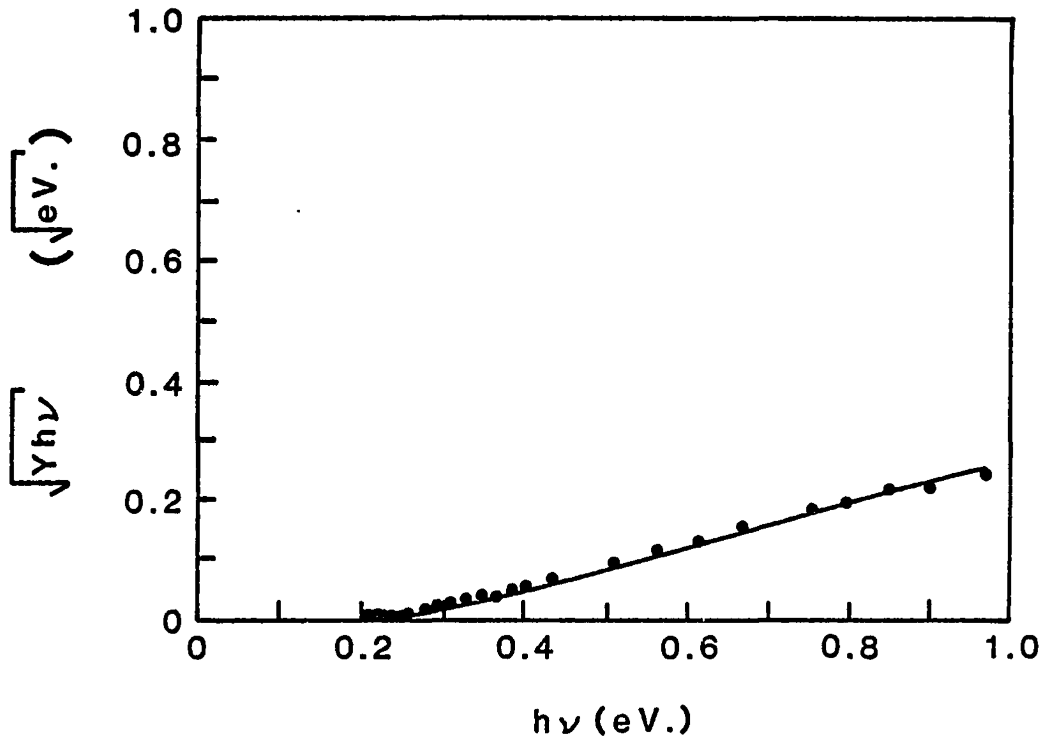

Figure 41(j). Similar to Figure 41(a) for diode 11.

The value of the partial merit function for this diode was 0.0240.

The mean free path between phonon collisions (L_p) was not addressed in section 3.3, and as usual, values of L_p for PtSi are not available in the literature. However L_p has been measured for Cd[41], Ga[42] and Al[43] at low temperatures ($T<11$ K). The results of these measurements show that L_p is dependent on the orientation of the carrier momentum with respect to the crystal lattice as well as on the temperature. The temperature dependence of L_p is found to vary as either $1/T^3$ or $1/T^5$. The $1/T^5$ dependence is attributed to multiple scatterings being required to significantly deflect the carriers[41,44]. Since the angular subtense of the escape cap is small, it is reasonable to assume that a single scatter is sufficient to scatter a carrier out of the escape cap, and thus the $1/T^5$ dependence is neglected. Extrapolating the $1/T^3$ results to 40 K, one finds the value of L_p to be in the range from 1,000 to 50,000 Å.

The one parameter value which has been measured for PtSi is the phonon energy (δ_p). In section 3.3 it was shown that the value of the phonon energy lies on the interval from 0.01 to 0.017 eV. Table 4 shows that the agreement between the best fit value and that of the literature is very good. The rest of the parameter values are reasonably consistent with the values obtained for other materials.

Table 5 lists the values of the imperfection mean-free-path for the ten diodes as well as the range over which

Table 4. The values of the parameters which are not affected by variations in processing.

parameter	value			
	-10%	best fit	+10%	
L_p	9.80×10^{3}	1.12×10^{4}	1.29×10^{4}	Å
δ_p	1.11×10^{-2}	1.40×10^{-2}	1.78×10^{-2}	eV
L_e	7.14×10^{4}	7.78×10^{4}	8.80×10^{4}	Å
τ	7.85×10^{-2}	7.85×10^{-2}	8.15×10^{-2}	
E_f	7.11	11.9	13.3	eV

they can vary and not impact the mean-squared-error by more than 10%. All but three of the diodes have L_i values which are consistent with those given in section 3.3 ($100 < L_i < 500$ Å). An examination of the process procedure for these three diodes showed that the metal deposition occurred at room temperature, while for the other seven diodes the deposition occurred at the anneal temperature.

Table 5. The values of L_i for each of the 10 diodes.

diode number	L_i (Å)		
	-10%	best fit	+10%
3	41,470	75,300	258,909
6	2,370	3,010	3,848
9	3,233	3,670	4,187
2	124	155	192
4	58.0	66.6	75.6
5	570	630	692
7	180	203	225
8	200	222	246
10	527	581	636
11	9.54	39.5	155

Chapter 6

CONCLUSIONS AND FUTURE WORK

Conclusions

The purpose of this work was to expand the theory of internal photoemission with the intent of explaining some of the puzzling features which existed on the Fowler plots of PtSi Schottky barrier infrared photodetectors. Figures 41 a-j show that the expanded model can fit the experimental Fowler plot data very well. Since the data is fit by the model, the four discrepancies between the simple model and the experimental data listed in section 2.4 are not present with the new model. Hence the puzzling features of the Fowler plots can be explained in terms of the physical processes considered in the extensions of the model. Specifically; the yields, which are higher than the simple model can explain without imposing very low values on E_f, are understood in terms of semi-elastic and elastic collisions which scatter the hot-hole into the escape cap. The roll off from linearity for high photon energies is due to the depletion of the spherical shell of emission. While both the finite yield for photon energies below the barrier and the discrepancy between the thermal and the optical

barriers are a result of the energy loss due to phonon creation.

By comparing the experimental data to the model, one can extract the values of the parameters used in the model. The extracted values were found to be in good agreement with the values in the literature for other materials. The values of $\hbar\omega$ and L_p' (the average energy loss and mean free path for semi-elastic scatters) were found to be linearly related. The linear relationship was physically modeled and exploited by reducing the number of free parameters per diode to one. With one free parameter per diode, any significant change in the processing can impact the diode's performance only by changing the value of one parameter.

The free parameter was physically interpreted as the mean free path between elastic scatters (L_i), and its value was found to be correlated to the temperature of the substrate when the platinum was deposited.

Future Work

It is recommended that future work proceed along two fronts. One can use the model in its present form to guide work on improving the photoresponse of the diodes, or one can further extend the model.

The photoresponse of the diodes can be improved by finding the combination of PtSi thickness and imperfection mean free path which gives the best quantum efficiency. Once this is accomplished, the problem becomes one of finding the processing procedure which gives the desired value of imperfection mean free path. As was shown in section 5.2, the temperature of the substrate during the deposition of the platinum might prove critical in tailoring this mean free path; however, the effects of the time and temperature of anneal should also be investigated.

The expansion of the model can proceed along any of a number of different paths. The accuracy of the model could be enhanced by including the effects of the dependence of the different parameters on the energy of the hot-hole, the nonuniformity in energy of the successive phonon distributions, as well as the nonuniformity in space of the optical excitation of the hot-holes.

Even though neglecting these effects presumably degrades the fit to the measured data, it would probably be more beneficial to measure some of the parameter values directly and independently (e.g. use the Sondheimer oscillation technique to measure the phonon mean free path in PtSi). The independently measured values could then be held fixed in the model and more reliable values for the other parameters extracted from the optimization routine.

REFERENCES

1. R. Williams, in Semiconductors and Semimetals, edited by R. K. Willardson and A. C. Beer, (Academic Press, New York, 1970), Vol. 6, pp. 97-139.

2. F. D. Shepherd and A. C. Yang, Proc. International Electron Devices Meeting p. 310 (1973).

3. R. H. Fowler, Phys. Rev. 38, 45 (1931).

4. V. L. Dalal, J. Appl. Phys. 42, 2274 (1971).

5. V. E. Vickers, Appl. Opt. 10, 2190 (1971).

6. H. B. Ghozlene, P. Beaufrere, A. Authier, J. Appl. Phys. 49, 3998 (1978).

7. O. S. Heavens, Thin Film Physics, (Methuen & Co. LTD and Science Paperbacks, London, 1970), p. 24.

8. S. M. Sze, Physics of Semiconductor Devices, 2nd ed. (John Wiley and Sons, New York, 1981), pp. 245-254.

9. J. Cohen, J. Vilms, R. J. Archer, "Investigation of Semiconductor Schottky Barriers for Optical Detection and Cathodic Emission," Final Report, AFCRL-68-0651, Dec. 1968 (Contract F19628-68-C-0090), Hewlett-Packard Labs., Palo Alto, Calif.

10. C. Kittel, Solid State Physics, 5th ed. (John Wiley and Sons, New York), p. 154.

11. Ref. 8, p. 262.

12. C. R. Crowell and S. M. Sze, J. Appl. Phys. 21, 2683 (1966).

13. C. Y. Chang and S. M. Sze, Solid-State Electron. 13, 727 (1970).

14. C. L. Anderson, C. R. Crowell, and T. W. Kao, Solid-State Electron. 18, 705 (1975).

15. J. M. Mooney and J. Silverman, IEEE Trans. Electron Devices ED-32, 33 (1985).

16. R. Stuart, F. Wooten, W. E. Spicer, Phys. Rev. Lett. 10, ZA518 (1963).

17. C. R. Crowell, W. G. Spitzer, H. G. White, Appl. Phys. Lett. 1, 3 (1962).

18. J. M. Ziman, Electrons and Phonons, (Clarendon Press, Oxford, 1960), pp. 412-418.

19. Ref. 10, p. 310.

20. J. J. Quinn, Phys. Rev. 126, 1453 (1962).

21. J. J. Quinn, Appl. Phys. Lett. 2, 167 (1963).

22. C. Hodges, H. Smith, J. W. Wilkins, Phys. Rev. B 4, 302 (1971).

23. D. B. Poker and C. E. Klabunde, Phys. Rev. B 26, 7012 (1982).

24. W. F. Krolikowski and W. E. Spicer, Phys. Rev. B 1, 478 (1970).

25. S. M. Sze, J. L. Moll, T. Sugano, Solid-State Electron. 7, 509 (1964).

26. J. C. Ashley, C. J. Tung, R. H. Ritchie, Surface Science 81, 409 (1979).

27. C. R. Crowell, W. G. Spitzer, L. E. Howarth, E. E. LaBate, Phys. Rev. 127, 2006 (1962).

28. S. M. Shivaparsad, L. A. Udachan, M. A. Angadi, Physics Lett. 21, 187 (1980).

29. J. C. Tsang, R. Matz, Y. Yokota, G. W. Rubloff, J. Vac. Sci. Technol. A2, 556 (1984).

30. J. C. Tsang, Y. Yokota, R. Matz, G. W. Rubloff, Appl. Phys. Lett. 44, 430 (1984).

31. C. W. Kao, C. L. Anderson, C. R. Crowell, Surafce Sci. 95, 321 (1980).

32. C. R. Crowell and S. M. Sze, Appl. Phys. Lett. 9, 242 (1966).

33. J. M. Pimbley and W. Katz, Appl. Phys. Lett. 42, 984 (1983).

34. G. D. Mahan and D. T. F. Marple, Appl. Phys. Lett. 42, 219 (1983).

35. K. L. Chopra, Thin Film Phenomena, (McGraw Hill, New York, 1969), p. 741.

36. O. S. Heavens, Optical Properties of Thin Solid Films, (Butterworths, London, 1955), p. 156.

37. J. E. Hubbs (private communication).

38. H. A. Macleod, Notes from a course given at the Optical Science Center, University of Arizona, Tucson Arizona, 1985 (unpublished).

39. C. D. Salzberg and J. J. Villa, J. Opt. Soc. Am. 47, 244 (1957).

40. M. S. Caceci and W. P. Cacheris, Byte 9, 340 (1984).

41. P. D. Hambourger, in Low Temperature Physics-LT13, (Plenum Press, New York and London, 1974), Vol. 4, p. 278.

42. J. A. Munarin, J. A. Marcus, P. E. Bloomfield, Phys. Rev. 172, 718 (1968).

43. H. Sato, J. Low Temp. Phys. 38, 267 (1980).

44. Ref. 18, p. 365.